ADVANCED SCIENCE Open Access
www.advancedscience.com

Inverse-Perovskite Ba_3BO (B = Si and Ge) as a High Performance Environmentally Benign Thermoelectric Material with Low Lattice Thermal Conductivity

Xinyi He, Shigeru Kimura, Takayoshi Katase, Terumasa Tadano, Satoru Matsuishi, Makoto Minohara, Hidenori Hiramatsu, Hiroshi Kumigashira, Hideo Hosono, and Toshio Kamiya**

High energy-conversion efficiency (ZT) of thermoelectric materials has been achieved in heavy metal chalcogenides, but the use of toxic Pb or Te is an obstacle for wide applications of thermoelectricity. Here, high ZT is demonstrated in toxic-element free Ba_3BO (B = Si and Ge) with inverse-perovskite structure. The negatively charged B ion contributes to hole transport with long carrier life time, and their highly dispersive bands with multiple valley degeneracy realize both high p-type electronic conductivity and high Seebeck coefficient, resulting in high power factor (PF). In addition, extremely low lattice thermal conductivities (κ_{lat}) 1.0–0.4 W m^{-1} K^{-1} at T = 300–600 K are observed in Ba_3BO. Highly distorted O–Ba_6 octahedral framework with weak ionic bonds between Ba with large mass and O provides low phonon velocities and strong phonon scattering in Ba_3BO. As a consequence of high PF and low κ_{lat}, Ba_3SiO (Ba_3GeO) exhibits rather high ZT = 0.16–0.84 (0.35–0.65) at T = 300–623 K (300–523 K). Finally, based on first-principles carrier and phonon transport calculations, maximum ZT is predicted to be 2.14 for Ba_3SiO and 1.21 for Ba_3GeO at T = 600 K by optimizing hole concentration. Present results propose that inverse-perovskites would be a new platform of environmentally-benign high-ZT thermoelectric materials.

1. Introduction

Due to the recently increasing energy crisis, there has been increasing attention to thermoelectric technology for power generation using waste heat energy.[1–3] The efficiency of thermoelectric energy conversion is governed by the dimensionless figure of merit (ZT), defined as $ZT = S^2 \cdot \sigma \cdot T \cdot \kappa^{-1}$, where T is the absolute temperature, S is the Seebeck coefficient, σ is the electronic conductivity, and κ is the thermal conductivity of the thermoelectric materials.[4–6] The product $S^2\sigma$ is known as the power factor (PF), and the κ includes the contributions from electronic (κ_{ele}) and lattice (κ_{lat}) heat conduction. Therefore, high ZT thermoelectric materials should exhibit large S and high σ to obtain high PF, as well as low κ to create a large temperature gradient. So far, the high ZT has been demonstrated mainly in heavy metal chalcogenides, such as Bi_2Te_3, PbTe, and GeTe,[7–9] which possess low κ_{lat}, but the use of toxic elements, such as Pb and Te, is not preferred for wide applications of thermoelectricity. There

X. He, S. Kimura, T. Katase, S. Matsuishi, H. Hiramatsu, H. Hosono, T. Kamiya
MDX Research Center for Element Strategy
International Research Frontiers Initiative
Tokyo Institute of Technology
4259 Nagatsuta, Midori, Yokohama 226-8501, Japan
E-mail: katase@mces.titech.ac.jp; kamiya.t.aa@m.titech.ac.jp

T. Tadano
Research Center for Magnetic and Spintronic Materials
National Institute for Materials Science
1-2-1 Sengen, Tsukuba, Ibaraki 305-0047, Japan

S. Matsuishi, H. Hosono
Research Center for Materials Nanoarchitectonics
National Institute for Materials Science
1-1 Namiki, Tsukuba, Ibaraki 305-0044, Japan

M. Minohara
Research Institute for Advanced Electronics and Photonics
National Institute of Advanced Industrial Science and Technology
Tsukuba, Ibaraki 305-8568, Japan

H. Hiramatsu
Laboratory for Materials and Structures
Institute of Innovative Research, Tokyo Institute of Technology
4259 Nagatsuta, Midori, Yokohama 226-8501, Japan

H. Kumigashira
Institute of Multidisciplinary Research for Advanced Materials
Tohoku University
Sendai 980-8577, Japan

The ORCID identification number(s) for the author(s) of this article can be found under https://doi.org/10.1002/advs.202307058

DOI: 10.1002/advs.202307058

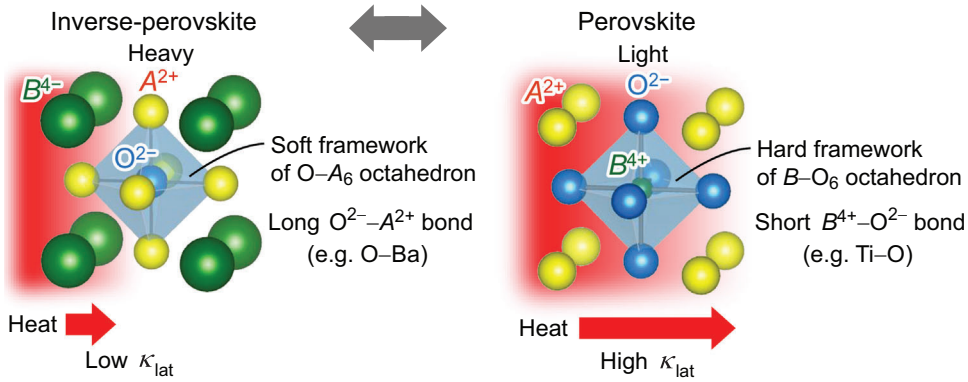

Figure 1. Schematic illustration of crystal structures and phonon transport in inverse-perovskite A_3BO (left) and normal perovskite ABO_3 (right). The normal perovskite structure of ABO_3 (e.g., $SrTiO_3$) is built with the hard framework of B–O_6 octahedron with short B–O bonds, providing high-density packing structure of the light element O^{2-} ions. In contrast, the inverse-perovskite structure of A_3BO (e.g., Ba_3BO (B = Si and Ge)) is constructed from the soft framework of O–A_6 octahedron with long O–A bonds, providing the high-density packing structure of heavy A^{2+} ions. The lattice thermal conductivity (κ_{lat}) of normal perovskite ABO_3 is usually high, while the largely contrasting structure characteristics are expected to lead the large reduction of κ_{lat} in inverse-perovskite A_3BO.

are many efforts on the development of environmentally benign thermoelectric materials, such as oxides, silicides, and sulfides,[10–14] but further exploration of novel material systems is demanded for improving the thermoelectric performance.

We herein focus on inverse-perovskite oxides as potential environmentally benign thermoelectric materials without toxic elements. The inverse-perovskite oxides are represented by chemical formula of A_3BO with formal ion charges of A^{2+} (alkaline earth = Ca^{2+}, Sr^{2+}, Ba^{2+}), B^{4-} (the p-block 14 group = Si^{4-}, Ge^{4-}, Sn^{4-}, Pb^{4-}), and O^{2-}.[15–20] It crystallizes in the inverse-perovskite structure that has an inverted cation and anion sites in comparison to the normal perovskite oxide ABO_3 ($A^{2+}B^{4+}O^{2-}$) such as $SrTiO_3$ (**Figure 1**). In the normal perovskite structure, B^{4+} cation occupies the body-centered site of the pseudo-cubic unit cell and O^{2-} anion occupies the face-centered sites, forming a B–O_6 octahedron. A^{2+} cation occupies the vertex sites of the unit cell. On the other hand, in the inverse-perovskite structure, O^{2-} anion occupies the body-centered site and the A^{2+} cation occupies the face-centered sites, forming an O–A_6 octahedron. B^{4-} anion occupies the vertex sites. ZT of perovskite $SrTiO_3$ is usually limited to ~0.1 due to its high κ_{lat} ≈10 W m^{-1} K^{-1} at room temperature (RT),[21] originating from the hard framework of the Ti–O_6 octahedra with the strong Ti–O bonds. In contrast, the inverse-perovskite structure is constructed from the soft framework of the O–A_6 octahedra because of the larger A^{2+} ion than B^{4+} ion and the consequent longer O–A bonds. From another point of view, normal perovskite $SrTiO_3$ is formed by the high-density packing structure of the light element O^{2-} ions, while inverse-perovskite A_3BO is formed by the high-density packing structure of heavier A^{2+} ions. These largely contrasting structural characteristics let us expect a large reduction of κ_{lat} in inverse-perovskite A_3BO. The most distinctive feature of inverse-perovskite A_3BO is that the B ion is negatively charged, which actively contributes to hole conduction; the localized O 2p state forms valence band maximum (VBM) in conventional oxides including normal perovskite oxides, while spatially spread p orbital of large-size B^{4-} anion (ion radius: > 2 Å of B^{4-}, 1.4 Å of O^{2-}) forms VBM in inverse-perovskite oxide,[22] which can realize high hole mobility and σ. Our work is hence motivated by the expectation that the inverse-perovskite oxide would be a potential candidate for high ZT thermoelectric materials.

The A_3BO with B = Sn and Pb adopts a high-symmetry cubic structure (*Pm*-3*m*) and exhibits unique Dirac electronic structures with high carrier mobility, being expected as a new class of topological crystalline insulators and superconductors.[22–26] However, their narrow bandgaps (theoretical bandgaps < 0.2 eV) limit their thermoelectric properties because the compensation by the coexistence of electrons and holes leads to low S, resulting in low PF at high temperatures.[27] On the other hand, theoretical studies proposed that bandgap is sensitive to structural distortion, which enhances the thermoelectric properties of inverse-perovskite A_3BO.[28–30] By replacing the B site with smaller Si and Ge ions, the cubic structure is distorted to an orthorhombic lattice in agreement with a smaller tolerance factor ($t = \frac{r_B+r_A}{2^{1/2}(r_O+r_A)}$) of an inverse-perovskite structure, where r_A, r_B, r_O are ionic radii for A, B, O ions.[28,31] The orthorhombic Ca_3SiO (Ca_3GeO) with t = 0.937 (0.948) takes the space group of *Imma* and increases the bandgap to 0.7–0.9 eV.[28,32] The thermoelectric properties were experimentally measured for Ca_3SiO and Ca_3GeO bulk polycrystals, which show low κ_{lat} = 1.0–1.9 W m^{-1}K^{-1} at RT but the obtained ZT are limited to less than 10^{-5} because the properties were measured with cold-pressed bulks with large amount of CaO impurity (24%–32% in the Ca_3SiO sample and 8%–10% in the Ca_3GeO sample).[33]

Here, we synthesized high-purity bulk polycrystals of highly distorted Ba_3BO (B = Si and Ge) with t = 0.908 and 0.918, which crystalize in orthorhombic inverse-perovskite structures (space group: *Pnma*) with the pronounced tilting and twisting of the O–Ba_6 octahedra (**Figure 2a**). The theoretical bandgaps are 0.86 eV for Ba_3SiO and 0.80 eV for Ba_3GeO. The undoped samples showed p-type degenerate conduction with hole concentrations ≈4.8 × 10^{18} cm^{-3} for Ba_3SiO and ≈6.2 × 10^{19} cm^{-3} for Ba_3GeO at RT. The bulk samples exhibited low κ_{lat} of 1.00 W m^{-1} K^{-1} for Ba_3SiO and 0.77 W m^{-1} K^{-1} for Ba_3GeO, which are lower than 1.7–2.0 W m^{-1} K^{-1} of Bi_2Te_3 and PbTe bulks at RT. Ba_3SiO and

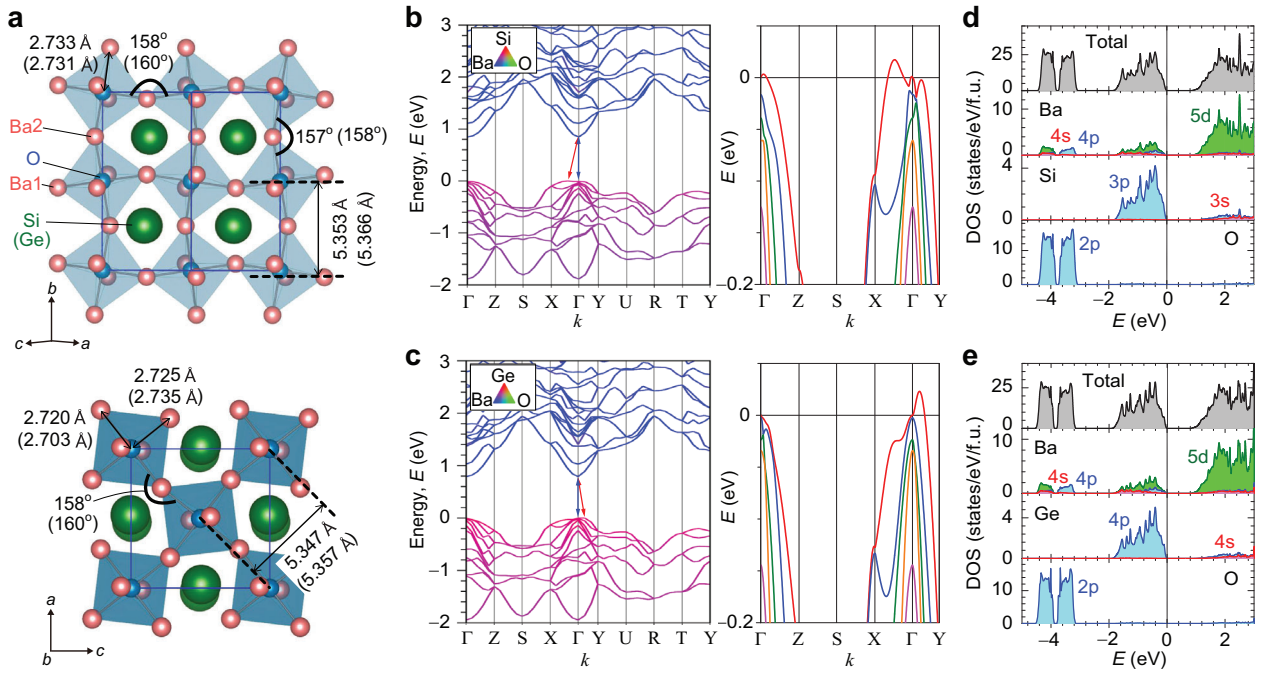

Figure 2. Crystal structure and electronic structure analyses of inverse-perovskite Ba_3BO (B = Si and Ge). a) Crystal structures of Ba_3SiO (Ba_3GeO) with space group of *Pnma*. The top and the bottom panels are the side view of (101) plane and the top view of (010) plane, respectively. b,c) Electronic band structures and d,e) partial density of states for b,d) Ba_3SiO and c,e) Ba_3GeO. The right panels of (b,c) are enlarged views of valence band maximum.

Ba_3GeO bulks exhibited relatively high $ZT = 0.16$ and 0.35 at RT, respectively, and the ZT value increased up to 0.84 for Ba_3SiO bulk at $T = 623$ K and 0.65 for Ba_3GeO bulk at $T = 523$ K. We systematically investigated the electronic and phonon transport properties of Ba_3BO by using first-principles calculations to clarify the underlying physical mechanisms for their low κ_{lat} and the potential of thermoelectric ZT.

2. Results and Discussion

2.1. Crystal Structure and Electronic Structure Analyses

The bulk polycrystals of Ba_3BO (B = Si and Ge) were synthesized by high-temperature solid-state reactions of 2Ba + Si(Ge) +BaO → $Ba_3SiO(Ba_3GeO)$. From X-ray diffraction (XRD) measurements, a small amount of BaO impurity (7.3 mol%) is detected for the Ba_3GeO bulk, and the weak unidentified diffraction peaks are observed for the Ba_3SiO bulk (Figure S1, Supporting Information, and CCDC 2291770 and 2291771 are the supplementary crystallographic data for this paper). Microstructure analysis by a field-emission scanning electron microscopy (FE-SEM) shows that the bulks are composed of sintered grains with an average grain size of ≈10 μm with some pores (Figure S2, Supporting Information), resulting in the sintered density of 80–87%. Energy dispersive X-ray spectroscopy (EDS) mapping confirms the uniformity of the chemical composition of Ba, Si (Ge), and O over the grain region. The orthorhombic lattice parameters estimated by Rietveld analysis of XRD patterns are $a = 7.581$ Å, $b = 10.706$ Å, $c = 7.543$ Å for Ba_3SiO and $a = 7.592$ Å, $b = 10.732$ Å, $c = 7.559$ Å for Ba_3GeO. Lattice volume is expanded from 612.261 Å^3 of Ba_3SiO to 615.896 Å^3 of Ba_3GeO because of the slightly larger ion radius of 2.08 Å for Ge^{4-} anion than 2.04 Å of Si^{4-} anion.[31] The pseudo-cubic lattice parameters of the orthorhombic unit cell for Ba_3SiO (Ba_3GeO) are $b/2 = 5.353$ Å (5.366 Å) and $\sqrt{a^2 + c^2} = 5.347$ Å (5.357 Å), indicating the O−Ba_6 octahedra are slightly elongated along the b-axis (Figure 2a). The orthorhombic distortion splits the Ba sites to the non-equivalent Ba1 and Ba2 sites. The O−Ba_6 octahedra are tilted and twisted around all three octahedral axes, where the apical O−Ba2−O and basal O−Ba1−O bond angles for Ba_3SiO (Ba_3GeO) are 157° (158°) and 158° (160°), showing distinct deviations from 180° of the cubic lattice.

Figure 2b-e summarizes electronic band structures and density of states (DOSs) of Ba_3BO calculated by the VASP[34,35] code with Heyd–Scuseria–Ernzerhof (HSE) hybrid functional.[36] The conduction band minimum (CBM) and VBM located around the Γ point (left panels of Figure 2b,c), where the difference in the k vector between direct and indirect bandgap (E_g) is small, as indicated by the blue and the red arrows. The E_g are calculated to be 0.86 eV for Ba_3SiO and 0.80 eV for Ba_3GeO, which are a little larger than the experimentally measured E_g of 0.62 eV and 0.58 eV (See diffuse reflectance spectra in Figure S3, Supporting Information), due to the E_g overestimation by HSE hybrid functional. The atomic charges estimated by the Bader charge analysis are $Ba^{+1.15}{}_3Si^{-2.02}O^{-1.45}$ and $Ba^{+1.14}{}_3Ge^{-1.99}O^{-1.45}$, confirming the anionic states of Si and Ge ions. The CBM is mainly contributed by the Ba 5*d* state with only one single valley at the Γ point, while the VBM arises primarily from the Si 3*p* (Ge 4*p*) state (Figure 2d,e). Specifically, the valence bands around the Γ point are composed of one flat band and four highly dispersive bands nearly degenerating within the 0.15 eV energy range below the Fermi level (right

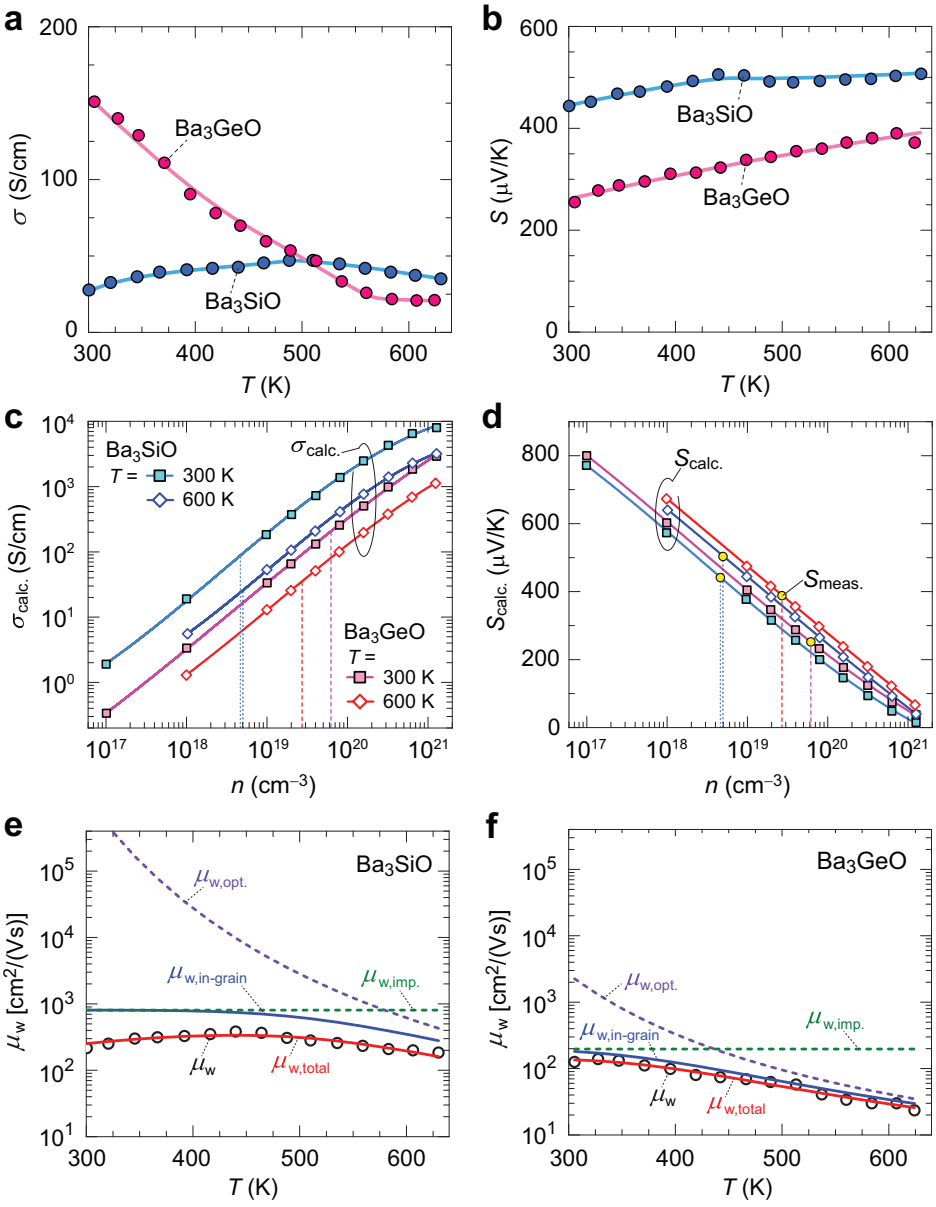

Figure 3. Carrier transport properties of Ba_3BO (B = Si and Ge). a,b) Temperature (T) dependences of a) electronic conductivity (σ) and b) Seebeck coefficient (S) of Ba_3BO bulks. c,d) Calculated electronic transport coefficients: c) $\sigma_{calc.}$ and d) $S_{calc.}$ as a function of carrier concentration (n) at T = 300 K and 600 K. The solid lines are the polynominal fitting to the data points of $\sigma_{calc.}$ vs n and $S_{calc.}$ vs n. The measured S ($S_{meas.}$) of Ba_3BO bulks are plotted in (d), and the dotted lines indicate the n estimated from the $S_{meas.}$ in the $S_{calc.}$ vs n relations. e,f) Weighted carrier mobility (μ_w) vs. T plots fitted by $\mu_{w,total}(T) = \exp(\frac{qE_b}{k_BT})\mu_{w,in-grain}(T)$, where $\mu_{w,in-grain}(T)$ is obtained by the Matthiessen's rule, $\mu^{-1}_{w,in-grain} = \mu^{-1}_{w,imp.} + \mu^{-1}_{w,opt.}$, for e) Ba_3SiO bulk and f) Ba_3SiO bulk. The red lines show the total mobility ($\mu_{w,total}$) and the blue lines show the in-grain μ_w without GB scattering ($\mu_{w,in-grain}$). The green and the purple dotted lines show the ionized impurity scattering limited mobility ($\mu_{w,imp.}$) and the optical phonon scattering limited mobility ($\mu_{w,opt.}$), respectively.

panels of Figure 2b,c). On the other hand, O 2p state located at a deeper energy level contributing little to carrier transport.

2.2. Carrier Transport Properties

Figure 3a,b shows the temperature (T) dependence of σ and S for Ba_3BO bulks. The Ba_3GeO bulk exhibits higher σ = 151 S cm^{-1} than 28 S cm^{-1} of Ba_3SiO bulk at $T \simeq$ 300 K (Figure 3a). The metallic T dependence of σ is observed for the Ba_3GeO bulk over the whole T range. On the other hand, σ of Ba_3SiO bulk shows metallic T dependence at high $T \geq$ 510 K, while σ decreases at $T <$ 500 K. Both the samples show positive S over the whole T range (Figure 3b), indicating the majority carrier is hole. The S = +444 μV K^{-1} for Ba_3SiO is larger than +255 μV K^{-1} for Ba_3GeO at $T \simeq$ 300 K. The S value linearly increases to +507 μV K^{-1} at T =

Table 1. Summary of experimentally measured and theoretically calculated carrier transport properties for Ba_3BO (B = Si and Ge) at T = 300 K and 600 K. m^*_{band} is the band effective mass and m^*_{DOS} is the density of state effective mass, calculated by BoltzTraP2 code. n is the carrier concentration obtained from the measured S in calculated $S_{calc.}$ vs n relation (Figure 3d). $\sigma_{meas.}$ is the experimentally measured electronic conductivity (Figure 3a). $\sigma_{calc.}$ is the calculated electronic conductivity obtained from the calculated $\sigma_{calc.}$ vs n relation at the estimated n (Figure 3c). μ and $\mu_{calc.}$ are the carrier mobility obtained by $\mu = \sigma_{meas.}/en$ and $\mu_{calc.} = \sigma_{calc.}/en$. τ_e and $\tau_{e,calc.}$ are the carrier life time obtained by $\tau_e = m^*_{band}\mu/e$ and $\tau_{e,calc.} = m^*_{band}\mu_{calc.}/e$.

	m^*_{band}	m^*_{DOS}	T [K]	n [cm^{-3}]	$\sigma_{meas.}$ [S cm^{-1}]	$\sigma_{calc.}$ [S cm^{-1}]	μ [cm^2 V^{-1} s^{-1}]	$\mu_{calc.}$ [cm^2 V^{-1} s^{-1}]	τ_e [fs]	$\tau_{e,calc.}$ [fs]
Ba_3SiO	$0.85m_0$	$2.46m_0$	300	4.8×10^{18}	28	89	36.4	115.7	17.6	55.9
			600	5.0×10^{18}	37	28	46.6	35.0	22.5	16.9
Ba_3GeO	$0.72m_0$	$2.24m_0$	300	6.2×10^{19}	151	195	15.2	19.6	6.2	8.0
			600	2.7×10^{19}	21	35	4.8	8.1	2.0	3.3

630 K for Ba_3SiO and +372 μV K^{-1} at T = 624 K for Ba_3GeO with increasing T. Note that Hall effect measurement was difficult to perform because these samples are sensitive to air and sample degradation occurs during the transfer to the measurement system.

We then calculated the carrier lifetime (τ_e) and obtained the carrier concentration (n) dependences of $\sigma_{calc.}$ and $S_{calc.}$ at T = 300 K and 600 K (Figure 3c,d) by density functional perturbation theory (DFPT)[37] as implemented in Quantum ESPRESSO package[38,39] and PERTURBO code.[40] It is seen that $\sigma_{calc.}$ increases while $S_{calc.}$ decreases with n as usually observed due to the well-known competitive relationship. The $\sigma_{calc.}$ of Ba_3SiO is nearly one order of magnitude higher than that of Ba_3GeO, which originates from the smaller τ_e in Ba_3GeO due to strong electron–phonon scattering (Figure S4, Supporting Information). Here, we need to compare $\sigma_{calc.}$ and the measured σ but $\sigma_{calc.}$ is a function of n. We, therefore, first estimated experimental n from the measured S ($S_{meas.}$) using the calculated $S_{calc.}$ vs n relation as a reference. We estimated n to be ≈4.8×10^{18} cm^{-3} (≈5.0×10^{18} cm^{-3}) for the Ba_3SiO bulk and ≈6.2×10^{19} cm^{-3} (≈2.7×10^{19} cm^{-3}) for the Ba_3GeO bulk at T = 300 K (600 K) as shown by the yellow circles in Figure 3d, indicating that the n of Ba_3SiO is one order of magnitude lower than that of Ba_3GeO. The n exhibits a weak T dependence for both the Ba_3SiO and the Ba_3GeO bulks, indicating degenerate hole conduction, which is supported by X-ray photo-emission spectroscopy spectra near the VBM (Figure S5, Supporting Information) because the Fermi level locates 0.1 eV below the VBM. We finally estimated $\sigma_{calc.}$ at the estimated n as the crossing points of the solid and dotted lines in Figure 3c.

Table 1 compares the experimentally measured and theoretically calculated carrier transport properties of Ba_3BO. Prior to explaining the detailed results, we like to summarize that the experimentally obtained results are consistent with the calculated ones both at T = 300 K and 600 K for Ba_3GeO while three times differences are found at T = 300 K for Ba_3SiO. For Ba_3GeO, the $\sigma_{calc.}$ (n at 300 K) = 195 S cm^{-1} and $\sigma_{calc.}$ (n at 600 K) = 35 S cm^{-1} are almost consistent with the measured σ ($\sigma_{meas.}$) = 151 S cm^{-1} at 300 K and 21 S cm^{-1} at 600 K, respectively. Accordingly, carrier mobility $\mu = \sigma_{meas.}/en$ and $\tau_e = m^*_{band}\mu/e$ (m^*_{band} is band effective mass) in Table 1 show similar consistency. On the other hand, for Ba_3SiO, although the $\sigma_{calc.}$ (n at 600 K) = 28 S cm^{-1} is consistent with $\sigma_{meas.}$ = 37 S cm^{-1} at T = 600 K, but $\sigma_{calc.}$ (n at 300 K) = 89 S cm^{-1} is three-times higher than $\sigma_{meas.}$ = 28 S cm^{-1} at T = 300 K. Accordingly, the estimated μ = 46.6 cm^2 V^{-1} s^{-1} is consistent with $\mu_{calc.}$ = 35.0 cm^2 V^{-1} s^{-1} at T = 600 K, while they show three-times difference (μ = 36.4 cm^2 V^{-1} s^{-1} and $\mu_{calc.}$ = 115.7 cm^2 V^{-1} s^{-1}) at 300 K. We here need to recognize that the calculated results reflect the transport properties of the ideal single crystal while the experimental ones include carrier scattering by defects and grain boundaries (GB), giving the significant discrepancy at lower temperatures.

To separate the single-crystalline-like carrier transport in crystalline grains and the effect of GBs, we employ the Seto model,[42] $\mu(T) = \exp(\frac{qE_b}{k_BT})\mu_{in-grain}(T)$, where $\mu_{in-grain}(T)$ is the in-grain carrier mobility and the GB contribution is expressed as $\exp(\frac{qE_b}{k_BT})$ (E_b is the GB barrier height and k_B is the Boltzmann constant). As we could not perform Hall effect measurements, we estimate $\mu(T)$ as weighted mobility from σ and S by $\mu_w = \frac{3h^3\sigma}{8\pi e(2m_ek_BT)^{3/2}}[\frac{exp[\frac{|S|}{k_B/e}-2]}{1+exp[-5(\frac{|S|}{k_B/e}-1)]} + \frac{\frac{3}{\pi^2}\frac{|S|}{k_B/e}}{1+exp[5(\frac{|S|}{k_B/e}-1)]}]$, where m_e is the free electron mass.[41] The μ_w is related to the drift mobility μ by $\mu_w \approx \mu(\frac{m^*_{DOS}}{m_e})^{3/2}$, where m^*_{DOS} is density of state effective mass. The μ_w of Ba_3SiO bulk exhibits a negative T coefficient at $T \geq$ 440 K, while it decreases with a decrease of T at low T region ≤ 440 K (the black circles in Figure 3e). The μ_w of Ba_3GeO bulk increases with a decrease of T in a wide range of $T \geq$ 327 K but it levels off at $T <$ 327 K (the black circles in Figure 3f). Then, $\mu_{w,in-grain}(T)$ is modeled by Matthiessen's rule, $\mu^{-1}_{w,in-grain} = \mu^{-1}_{w,imp.} + \mu^{-1}_{w,opt.}$. The impurity scattering mobility is expressed as $\mu^{-1}_{w,imp.}$ = A (temperature independent) in the degenerate regime. The optical phonon scattering mobility is expressed as $\mu^{-1}_{w,opt.} = 1/(B(\exp(\frac{\hbar\omega_0}{kT}) - 1))$ (B is a constant), where $\hbar\omega_0$ is the longitudinal optical phonon energy. These parameters are obtained by least-squares fitting of the total mobility $\mu_{w,total}(T) = \exp(\frac{qE_b}{k_BT})\mu_{w,in-grain}(T)$ to the experimental $\mu_w(T)$. In Figure 3e,f, the solid red line shows the $\mu_{w,total}$ providing good agreement with experimental μ_w over a wide T range. At high T region, the $\mu_{w,in-grain}$ (blue lines) is dominated by optical phonon scattering (the purple dotted lines), where the $\hbar\omega_0$ values were optimized to be 260 meV for Ba_3SiO and 210 meV for Ba_3GeO. The $\mu_{w,in-grain}$ increases and approaches the $\mu_{w,imp.}$ (green dotted lines), when T is reduced to ≈300 K. The $\mu_{w,in-grain}$ is higher than $\mu_{w,total}$ especially at lower T range for Ba_3SiO bulk, indicating that the carrier transport is limited by GB scattering. The $\mu_{w,in-grain}$ is 3.2 times higher than $\mu_{w,total}$ at $T \simeq$ 300 K, which is consistent with the $\mu_{calc.}/\mu$ = 3.2 obtained in Table 1. For Ba_3GeO, the $\mu_{w,in-grain}$ is nearly the same with $\mu_{w,total}$ in a wide range of $T \geq$ 327 K but the difference becomes a little larger at $T <$ 327 K. The $\mu_{w,in-grain}$ is 1.3 times higher than $\mu_{w,total}$

at $T \simeq 300$ K, in consistence with the $\mu_{calc.}/\mu = 1.3$. The E_b is estimated to be 28 meV for Ba_3SiO while $E_b = 8$ meV is much smaller for Ba_3GeO. The higher density carriers in Ba_3GeO bulk may screen the GB background charges and reduce the GB barrier heights. Although the Ba_3BO bulks have a relatively poor polycrystalline nature with low sintered densities 80–87% and the carrier transport of Ba_3SiO bulk is limited by GB scattering at low T region, the mobility analysis suggests that Ba_3BO possess potentially high carrier mobility.

Next, effective masses m^* are estimated as m^* determines S in the simple free electron model by $S = \frac{k_B}{e}(\frac{3}{2}\ln m^*_{DOS} + \ln 2(\frac{2\pi k_B T}{h^2})^{\frac{3}{2}} + r + 2 - \ln n)$, where m^*_{DOS} is the density-of-states effective mass at VBM. Here the band effective masses ($m^*_{band} = Ne^2\frac{\tau_e}{\sigma}$) at VBM are calculated to be slightly large at $0.85m_0$ for Ba_3SiO and $0.72m_0$ for Ba_3GeO (Table 1). However, the calculated carrier lifetime ($\tau_{e,calc.}$) is long at 55.9 fs for Ba_3SiO and 8.0 fs for Ba_3GeO, resulting in the relatively high $\mu_{calc.}$ of 115.7 and 19.6 $cm^2\ V^{-1}\ s^{-1}$ at $T = 300$ K, respectively. The dispersive bands at VBM with relatively small m^*_{band} and long τ_e contribute to high μ ($= \frac{e\tau_e}{m^*_{band}}$) and σ ($= \mu ne$). However, the lifetime calculations were performed at the rigid band scheme (no ion dynamics) and polaron effect is not considered but it can reduce the real μ. On the other hand, m^*_{DOS} are calculated to be $2.46m_0$ for Ba_3SiO and $2.24m_0$ for Ba_3GeO. The large m^*_{DOS} originates from the high valence band degeneracy as explained for Figure 2b,c, which contributes to the large S. Therefore, the negatively-charged B ion contributes to hole transport with long carrier life time, and the dispersive valence bands (small m^*_{band}) with the high valley degeneracy (large $m_{DOS}{}^*$) are suitable for realizing high PF ($= S^2\sigma$).

2.3. Thermal Transport Properties

Next we discuss thermal transport properties by separating electronic and lattice contributions. **Figure 4a** summarizes the T dependence of total κ (κ_{total}) and electronic κ (κ_{ele}) of Ba_3SiO and Ba_3GeO bulks. The κ_{ele} is calculated by Wiedemann-Franz law as $\kappa_{ele} = LT\sigma$, where L is the Lorenz number calculated from $L = (\frac{k_B}{e})^2(\frac{(r+\frac{7}{2})F_{r+5/2}(\eta)}{(r+\frac{3}{2})F_{r+\frac{1}{2}}(\eta)} - [\frac{(r+\frac{5}{2})F_{r+3/2}(\eta)}{(r+\frac{3}{2})F_{r+1/2}(\eta)}]^2)$. Here, the reduced Fermi energy η is obtained based on the free carrier model using the measured S as $S = \frac{k_B}{e}(\frac{(r+\frac{5}{2})F_{r+3/2}(\eta)}{(r+\frac{3}{2})F_{r+1/2}(\eta)} - \eta)$ with the Fermi integral defined as $F_n(\eta) = \int_0^\infty \frac{\chi^n}{1+e^{\chi-\eta}}d\chi$, where $\gamma = -1/2$ is the scattering factor.[43] The Ba_3SiO and Ba_3GeO bulks showed low κ_{total} of 1.02 $W\ m^{-1}K^{-1}$ for Ba_3SiO and 0.84 $W\ m^{-1}K^{-1}$ for Ba_3GeO at $T = 300$ K. The κ_{total} values of Ba_3SiO and Ba_3GeO bulks decrease to 0.69 $W\ m^{-1}K^{-1}$ and 0.43 $W\ m^{-1}K^{-1}$ as the T rises to 623 K. The estimated κ_{ele} was less than 0.1 $W\ m^{-1}K^{-1}$, where the maximum κ_{ele} was 0.04 $W\ m^{-1}K^{-1}$ at $T = 523$ K for Ba_3SiO and 0.07 $W\ m^{-1}K^{-1}$ at $T = 300$ K for Ba_3GeO, indicating the small electronic contribution to κ_{total}. Then, the lattice κ (κ_{lat}) is extracted by subtracting the electronic contribution from the κ_{total}, i.e. $\kappa_{lat} = \kappa_{total} - \kappa_{ele}$. The T dependences of κ_{lat} are summarized in Figure 4b, where those of the normal perovskite $SrTiO_3$ bulk[44] as well as representative chalcogenides of Bi_2Te_3 and PbTe bulks[45–47] are superimposed for comparison. The κ_{lat} decreases from 1.00 $W\ m^{-1}\ K^{-1}$ at $T = 300$ K to 0.66 $W\ m^{-1}\ K^{-1}$ at $T = 623$ K for Ba_3SiO and it decreases from 0.77 $W\ m^{-1}\ K^{-1}$ at RT to 0.41 $W\ m^{-1}\ K^{-1}$ at $T = 623$ K for Ba_3GeO. The κ_{lat} at $T = 300$ K is much lower than 8.2 $W\ m^{-1}\ K^{-1}$ of $SrTiO_3$ bulk[44] and also even lower than ≈1.7 $W\ m^{-1}\ K^{-1}$ of Bi_2Te_3 bulk[45] and ≈2.0 $W\ m^{-1}\ K^{-1}$ of PbTe bulk,[47] while it is comparable to κ_{lat} of state-of-the-art chalcogenide thermoelectric materials, such as 0.7 $W\ m^{-1}K^{-1}$ of SnSe bulk,[48] 0.6 $W\ m^{-1}K^{-1}$ of Cu_2Se bulk,[49] and 0.6–0.8 $W\ m^{-1}K^{-1}$ of GeTe bulk.[7]

2.4. Origin of Low Lattice Thermal Conductivity in Inverse-Perovskite

We compared the phonon transport properties of Ba_3BO with the normal perovskite $SrTiO_3$ to discern the distinguishing characteristics of inverse perovskites. First, we performed the simple phonon gas model analysis using $\kappa_{lat} = \frac{1}{3}C_v \cdot v_s \cdot l_{ph} = \frac{1}{3}C_v \cdot v_s^2 \cdot \tau_{ph}$, where C_v is the specific heat per volume, v_s is the sound velocity, l_{ph} is the phonon mean free path, and τ_{ph} is the phonon lifetime (Table S1, Supporting Information). The v_s, measured by ultrasonic pulse echo method at RT, are 2317 $m\ s^{-1}$ (1981 $m\ s^{-1}$) for Ba_3SiO (Ba_3GeO), which is less than a half of 5241 $m\ s^{-1}$ for the normal perovskite $SrTiO_3$. In addition, the estimated τ_{ph} of 0.16 ps (0.16 ps) for Ba_3SiO (Ba_3GeO) is a half of 0.32 ps of $SrTiO_3$. The smaller v_s and lower τ_{ph} lead to the shorter l_{ph} ($= v_s\tau_{ph}$) of 0.38 nm (0.32 nm) for Ba_3SiO (Ba_3GeO) than 1.70 nm for $SrTiO_3$, resulting in the low κ_{lat}. The bulk modulus was calculated to be 92.8 GPa (80.0 GPa) and the Debye temperature was 220 K (187 K) for Ba_3SiO (Ba_3GeO). The estimated Grüneisen parameter was relatively large at 1.3–1.4, which is comparable to low κ_{lat} thermoelectric materials such as Bi_2Te_3 and PbTe,[50] Therefore, both the low sound velocity and the strong phonon scattering are responsible for the intrinsically low κ_{lat} in Ba_3BO.

To further elucidate the underlying mechanism responsible for the low κ_{lat} in Ba_3BO, we conducted first-principles anharmonic lattice dynamics (ALD) calculations based on the density functional theory (DFT), as implemented in the ALAMODE code.[52,53] Figure 4c,d compares the anharmonic phonon dispersions (left panels) and the partial phonon DOSs projected on each element (right panels) for Ba_3BO and $SrTiO_3$ models at $T = 300$ K. Ba_3BO exhibits flatter phonon bands and all phonon bands only exist at a low frequency below 9 THz (left panel of Figure 4c). The phonon DOSs of the Ba_3SiO reveal that the vibrations of Ba atoms predominantly contribute to the lower frequency phonon bands with the cut-off frequency ≈4.3 THz, while the Si and O atoms primarily contribute to higher frequency phonon branches (right panel of Figure 4c). For Ba_3GeO, the phonon bands of heavier Ge ion shift to lower frequency and have interaction with the phonon bands of Ba ion. On the other hand, $SrTiO_3$ exhibits largely dispersive phonon bands even at higher frequencies (left panel of Figure 4d), with extensive dispersion at high frequencies of 4–14 THz, originating from the cooperative Ti and O atomic vibration (right panel of Figure 4d). The dispersion is considerably larger than observed in the low-frequency phonon bands primarily attributed to Sr atomic vibrations at frequencies below ≈4.3 THz.

We then calculated κ_{lat} by solving the Peierls–Boltzmann transport equation (PBTE) within the relaxation time approximation. The calculated κ_{lat} (averaged along a,b,c-axes) as a function of T

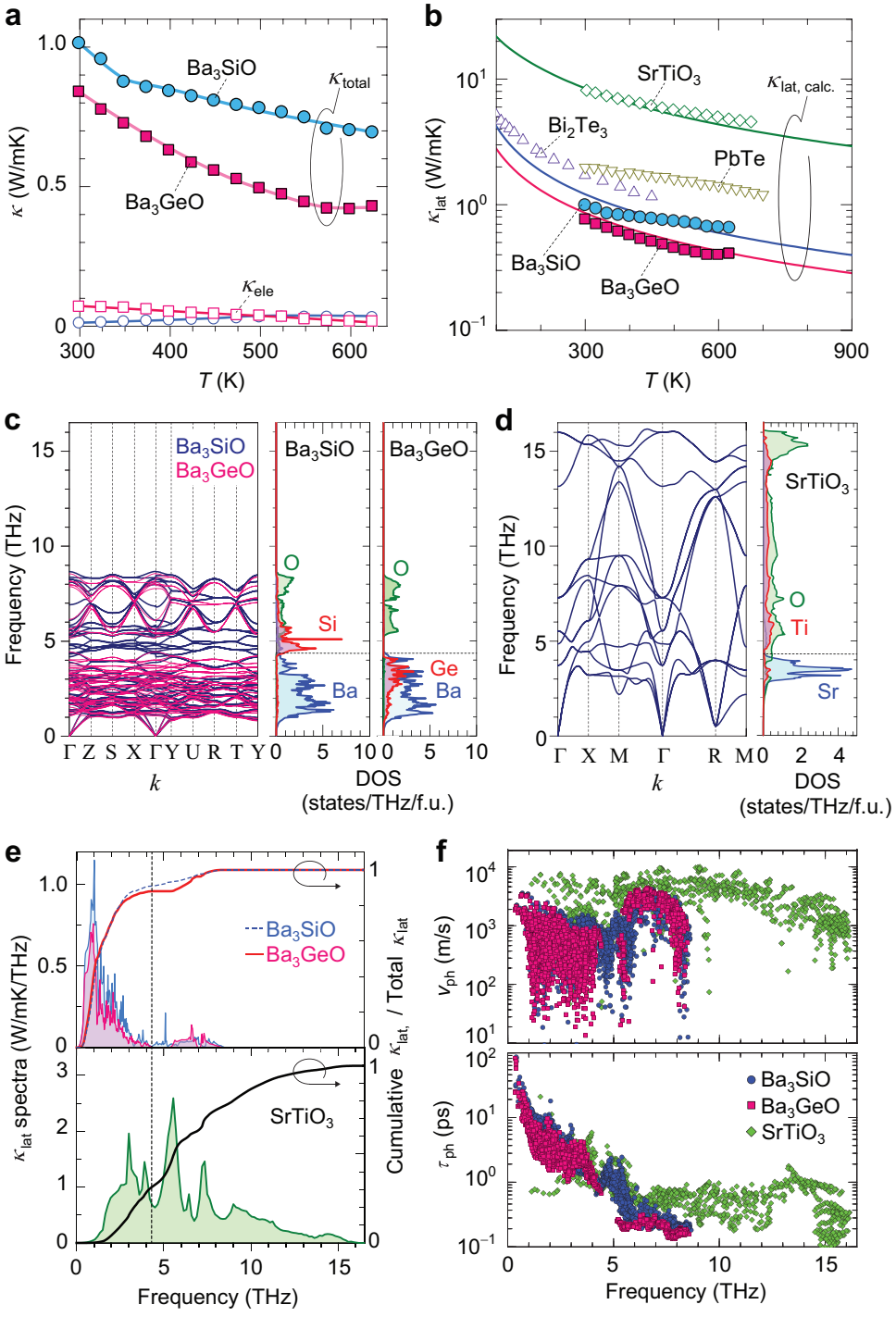

Figure 4. Phonon transport properties of Ba_3BO (B = Si and Ge). a) Temperature (T) dependences of total thermal conductivity (κ_{total}) and electronic thermal conductivity (κ_{ele}) for Ba_3BO bulks. b) T dependence of lattice thermal conductivity (κ_{lat}) for Ba_3BO bulks, compared with the reported κ_{lat} of normal perovskite $SrTiO_3$ bulk[44] as well as PbTe and Bi_2Te_3 bulks.[45–47] Calculated κ_{lat} of Ba_3BO and $SrTiO_3$ models are also shown by the solid lines. c,d) Anharmonic phonon dispersions (left panel) and partial phonon density of states (DOSs) projected on each element (right panel) for c) Ba_3BO and d) $SrTiO_3$ at $T = 300$ K obtained by the self-consistent phonon (SCPH) approximation. e) Comparison of κ_{lat} spectra for Ba_3BO (top panel) and $SrTiO_3$ (bottom panel) at $T = 300$ K. Frequency-dependent cumulative κ_{lat} normalized by total κ_{lat} is also shown for each panel. f) Phonon group velocity, v_{ph} (top panel), and phonon lifetime, τ_{ph} (bottom panel) in terms of the phonon frequency.

for Ba_3BO and $SrTiO_3$ are compared in Figure 4b. The calculated κ_{lat} of Ba_3SiO (Ba_3GeO) are 1.21 W m^{-1} K^{-1} (0.86 W m^{-1} K^{-1}) and that of $SrTiO_3$ is 8.46 W m^{-1} K^{-1} at T = 300 K, in consistence with the experimentally measured values. Figure 4e compares the κ_{lat} spectra at T = 300 K with respect to phonon frequency for Ba_3BO and $SrTiO_3$ models. The frequency-dependent cumulative κ_{lat} normalized by total κ_{lat} are also shown in the panels. For Ba_3BO, the κ_{lat} spectra peak at ≈1 THz and phonons in the low-frequency region below ≈4.3 THz contribute mostly to κ_{lat}. The acoustic and optical modes are hybridized when the q point is far from the Γ point, making it difficult to distinguish the acoustic and optical contributions clearly. However, if we consider a cut-off frequency for acoustic phonons, at which the acoustic and optical branches cross (Figure 4c), at ≈1.4 THz for Ba_3BO, the contribution of low-frequency acoustic phonons to κ_{lat} is ≈55%. The low-frequency acoustic phonons and mid-frequency optical phonons within 4.3 THz contribute to the ≈91% of total κ_{lat}, indicating that heat conduction primarily arises from the vibrational motion of Ba atoms (also Ge atoms in Ba_3GeO). In contrast, for $SrTiO_3$, the low-frequency acoustic phonons and mid-frequency optical phonons within 4.3 THz contribute to only the ≈31% of total κ_{lat}, i.e., not only the low-frequency Sr atom vibrations but also high-frequency phonons associated with Ti and O atomic vibrations contribute greatly to heat conduction.

Figure 4f compares the phonon group velocity, ν_{ph} (top panel) and phonon lifetime, τ_{ph} (bottom panel) in terms of the phonon frequency. Ba_3BO exhibit much lower ν_{ph} than $SrTiO_3$ across all frequency ranges, primarily due to the presence of flat phonon band branches (left panel of Figure 4c). On the other hand, τ_{ph} is almost similar at low frequency (<3.5 THz) for both Ba_3BO and $SrTiO_3$, but the value of Ba_3BO becomes smaller at higher frequency region (3.5–5 THz). For $SrTiO_3$, the τ_{ph} becomes smaller at high frequency (>6 THz), but ν_{ph} is still large, reflecting the widely spread optical phonon bands. Therefore, the large ν_{ph} for phonons associated not only with Sr atomic vibration but also with Ti and O atomic vibrations provides a large contribution to high κ_{lat} in $SrTiO_3$. The τ_{ph} of Ba_3BO becomes further smaller in the higher frequency region. The low κ_{lat} of Ba_3BO predominantly originates from the low ν_{ph} for phonons associated with Ba atomic vibration, and the phonons associated with Si and O atomic vibrations have a negligible contribution to κ_{lat} due to the very short τ_{ph}. Ba_3BO shows more phonon bands than $SrTiO_3$ (left panel of Figure 4c), because it has the local structure distortion with lower crystalline symmetry, resulting in the splitting of degenerated phonon bands. These broad frequency shifts enhance the phonon-phonon scattering probability that leads to a large τ_{ph} reduction in Ba_3BO. The inverse and the normal perovskite structures are constructed from the network of O−Ba_6 and Ti−O_6 octahedra. Then, the bonding energies of O−Ba in Ba_3BO and Ti−O in $SrTiO_3$ as a measure of bonding strengths were estimated through the chemical bonding analysis using the crystal orbital Hamilton population (COHP)[53] performed by the LOBSTER code.[54] For the Ba_3BO case, the −iCOHP values (the integrated −COHP up to the Fermi level, corresponding to the bond strength) averaged for O−Ba bonds are as small as 0.276 eV per bond for Ba_3SiO and 0.283 eV per bond for Ba_3GeO, indicating ionic interaction between the Ba atom and O atom in O−Ba_6 octahedra of the Ba_3BO. On the other hand, the Ti−O bonds of $SrTiO_3$ have more than 10 times larger −iCOHP values of 3.48 eV per bond, originating from the strong covalent interaction between the Ti atom and the O atom in $SrTiO_3$ lattice. The inverse-perovskite Ba_3BO has a similar crystal structure to the perovskite $SrTiO_3$, but the ionic nature of the O−Ba bond softens the octahedra framework and thus the contribution of high-frequency optical phonons is negligible for heat transport in Ba_3BO. Note that the related phenomenon of low κ_{lat} and strong phonon scattering is observed in layered BaAgSb with weakly ionic bonded Ba atoms.[55]

2.5. Thermoelectric Properties

Figure 5a,b summarizes the T dependences of PF (= $S^2\sigma$) and ZT (= $S^2\sigma T/\kappa$) of the Ba_3BO bulks. The calculated PF ($PF_{calc.}$ = $S^2\sigma_{calc.}$) and ZT ($ZT_{calc.}$ = $S^2\sigma_{calc.}T/\kappa_{calc.}$) are also superimposed in the panel. The PF of Ba_3SiO and Ba_3GeO bulks are limited to 5.5 and 9.8 μW cm^{-1} K^{-2} at $T \simeq$ 300 K, respectively, because of GB scattering (Figure 5a), but, as a consequence of their low κ, Ba_3SiO and Ba_3GeO show relatively high ZT = 0.16 and 0.35 at $T \simeq$ 300 K, respectively (Figure 5b). On the other hand, they potentially show higher $PF_{calc.}$ = 17.3 and 12.4 μW cm^{-1} K^{-2} by eliminating GB scattering, and $ZT_{calc.}$ would be increased up to 0.44 and 0.40 for Ba_3SiO and Ba_3GeO, respectively. The PF of Ba_3SiO largely increases to 11.6 μW cm^{-1} K^{-2} when T increases to 464 K, and then decreases to 9.0 μW cm^{-1} K^{-2} at high T = 630 K. The ZT value increases continuously up to 0.84 at T = 623 K, which is slightly higher than $ZT_{calc.}$ = 0.65 at T = 600 K due to higher σ than $\sigma_{calc.}$ On the other hand, Ba_3GeO exhibits the maximum PF = 10.8 μW cm^{-1} K^{-2} at low T = 327 K, and the PF decreases continuously down to 5.9 μW cm^{-1} K^{-2} at T = 523 K, where the maximum ZT = 0.65 was obtained. The $ZT_{calc.}$ of Ba_3GeO increases continuously up to 0.74 at T = 600 K, but the PF and ZT suddenly decrease at $T \geq$ 548 K due to the decrease of σ (Figure 3a) and the increase of κ (Figure 4a). We speculate that these σ and κ changes of Ba_3GeO would originate from the transition to higher symmetric inverse-perovskite structure at high T because it has slightly high tolerance factor = 0.918. The high T crystal-structure characterization is necessary for this conclusion.

Note that we tried hole doping to obtain optimum ZT by potassium ion (K^+) substitution for Ba_3SiO. The σ is increased by K doping and the two-orders of magnitude increase of carrier concentration is observed in $(Ba_{2.6}K_{0.4})SiO$. However, a considerably large amount of K dopant is necessary to increase the carrier concentration and also carrier mobility is largely suppressed by such heavy K doping. Therefore, further exploration of efficient acceptor dopants is necessary to optimize their ZT. Instead, we estimate the maximum ZT of Ba_3BO with optimized n theoretically. We here calculate $PF_{calc.}$ and $ZT_{calc.}$ as a function of n (Figure 5c,d). The $PF_{calc.}$ vs n and $ZT_{calc.}$ vs n plots have maxima with respect to n, and the maximum values (max $PF_{calc.}$ and max $ZT_{calc.}$) are obtained at optimal n ($n_{opt.}$) as indicated by the arrows in Figure 5c,d. The $n_{opt.}$ are estimated to be 4.0 (8.1) × 10^{19} cm^{-3} and 1.6 (1.6) × 10^{20} cm^{-3} for Ba_3SiO and Ba_3GeO at T = 300(600) K. **Table** 2 summarizes the theoretical thermoelectric properties of Ba_3BO with $n_{opt.}$ at T = 300 and 600 K. The max $ZT_{calc.}$ of Ba_3SiO is predicted to be 0.98 and 2.14 at T = 300 and 600 K, respectively, where the max $PF_{calc.}$ are much increased to 48.0 and 28.9 μW cm^{-1} K^{-2} by tuning n to $n_{opt.}$. The

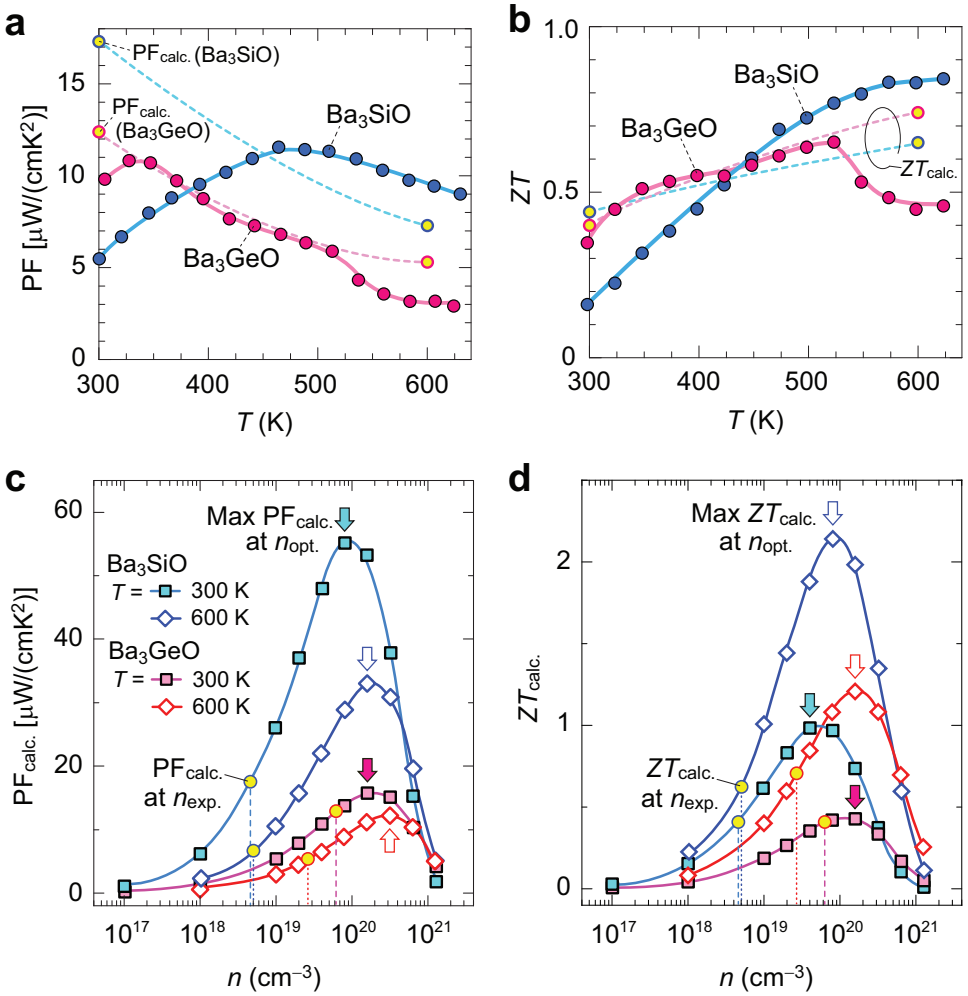

Figure 5. Thermoelectric properties of Ba_3BO (B = Si and Ge). a,b) Temperature (T) dependences of a) power factor (PF) and b) dimensionless figure of merit (ZT) of Ba_3BO bulks. c,d) Carrier concentration (n) dependences of c) calculated PF ($PF_{calc.} = S^2\sigma_{calc.}$) and d) calculated ZT ($ZT_{calc.} = S^2\sigma_{calc.}T/\kappa_{calc.}$) at T = 300 K and 600 K. The arrows indicate the maximum $PF_{calc.}$ and $ZT_{calc.}$ at the optimal n ($n_{opt.}$). The yellow circles in a-d indicate the $PF_{calc.}$ and $ZT_{calc.}$ obtained from the experimental n ($n_{exp.}$) estimated in Figure 3d.

max $ZT_{calc.}$ of Ba_3GeO are predicted to be 0.43 and 1.21 at T = 300 K and 600 K, respectively, where the max $PF_{calc.}$ is increased to 15.8 and 11.2 μW cm^{-1} K^{-2}. The higher ZT of Ba_3SiO compared with Ba_3GeO accounts for its higher PF. **Figure 6** compares the present maximum predictions for Ba_3SiO and Ba_3GeO with state-of-the-art thermoelectric materials. The max $ZT_{calc.}$ value of Ba_3SiO is much higher than those of eco-friendly thermoelectric materials[56–82] as seen in Figure 6a. Although higher ZT has been reported for the thermoelectric materials with heavy toxic elements of Pb, Te, Se, and Sb,[49,83–136] the max $ZT_{calc.}$ value of Ba_3SiO is comparable in the same temperature range (Figure 6b). For fair discussion, we like to note that these predictions are of ideal single crystals so the real maximum values would be reduced a bit by the impurity doping and consequent electron scattering. The present results, nonetheless, demonstrate the potential of inverse-perovskite Ba_3BO as a high-performance environmentally benign thermoelectric material that can be alternative to currently practical ones composed of heavy and toxic elements.

Table 2. Summary of theoretical thermoelectric properties for Ba_3BO (B = Si and Ge) with optimal n ($n_{opt.}$) at T = 300 K and 600 K.

	T [K]	$n_{opt.}$ [cm^{-3}]	$\sigma_{calc.}$ [S cm^{-1}]	$S_{calc.}$ [μV K^{-1}]	$PF_{calc.}$ [μW cm^{-1} K^{-2}]	$\kappa_{calc.}$ [W m^{-1} K^{-1}]	$\kappa_{ele,calc.}$ [W m^{-1} K^{-1}]	$\kappa_{lat,calc.}$ [W m^{-1} K^{-1}]	$ZT_{calc.}$
Ba_3SiO	300	4.0×10^{19}	726.7	+257	48.0	1.46	0.25	1.21	0.98
	600	8.1×10^{19}	411.2	+265	28.9	0.81	0.21	0.60	2.14
Ba_3GeO	300	1.6×10^{20}	503.5	+177	15.8	0.86	0.25	0.86	0.43
	600	1.6×10^{20}	197.2	+238	11.2	0.43	0.13	0.43	1.21

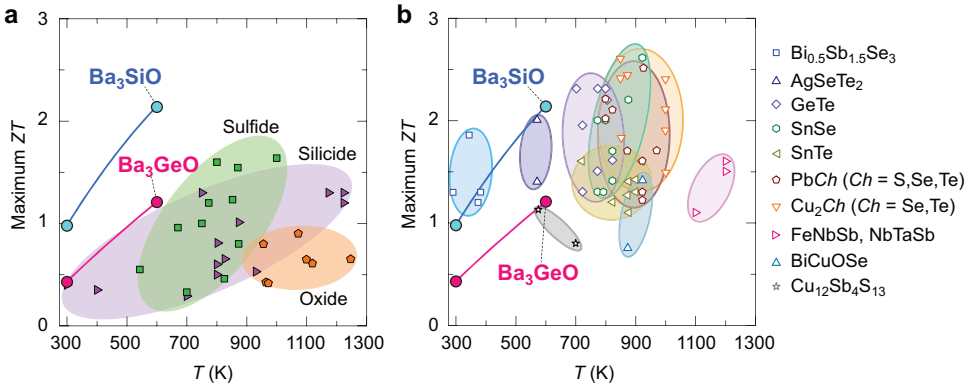

Figure 6. Comparison of maximum ZT as a function of temperature (T) for Ba_3BO (B = Si and Ge) with respect to a) eco-friendly thermoelectric materials including sulfides (Cu_2S,[56–59] SnS,[60] $Cu_{0.1}TiS_2$,[61] $(Cu,Fe)S_2$,[62] $Cu_7Sn_3S_{10}$,[63] Cu_5FeS_4,[64] $Cu_{26}Ta_2Sn_{5.5}S_{32}$,[65] Cu_2ZnSnS_4[66]), silicides ($Si_{0.8}Ge_{0.2}$,[67] Mg_2Si,[68–70] $Mg_2(Si,Sn)$,[71] $MnSi_{1.75}$,[72] $CrSi_2$,[73] β-$FeSi_2$,[74] $Sr_{0.92}Y_{0.08}Si_2$[75]), oxides ($Sr_{0.9}La_{0.1}Ti_{0.9}Nb_{0.1}O_3$,[76] $Sr_{0.93}La_{0.07}Ti_{0.93}Nb_{0.07}O_3$,[77] $Sr_{0.775}La_{0.15}\square_{0.075}TiO_{3-\delta}$,[78] $Zn_{0.96}Al_{0.02}Ga_{0.02}O$,[79] $Na_{1.7}Co_2O_4$,[80] $Ca_{2.8}Ag_{0.05}Lu_{0.15}Co_4O_{9+\delta}$,[81] $Ca_{2.95}Tb_{0.05}Co_4O_9Bi_{0.25}$[82]), and b) state-of-the-art thermoelectric materials with heavy (toxic) elements: $Bi_{0.5}Sb_{1.5}Se_3$,[83–86] $AgSeTe_2$,[87,88] GeTe,[89–96] SnSe,[97–104] SnTe,[105–112] PbCh (Ch = S, Se, Te),[113–121] Cu_2Ch (Ch = Se, Te),[49,122–129] Half Heusler FeNbSb and FeTaSb,[130–132] BiCuOSe,[133,134] Tetrahedrite $Cu_{12}Sb_4S_{13}$.[135,136] Green, purple, and orange symbols in (a) indicate maximum ZT values for sulfide, silicide, and oxide thermoelectric materials, respectively.

3. Conclusion

In summary, we demonstrated the high ZT in bulk polycrystals of the p-type inverse-perovskite Ba_3BO (B = Si and Ge) without toxic elements. The valence band around the Fermi level arises from the p state of the negatively charged B anion with large ion size, and the hole transport with long carrier life time and their highly dispersive bands with multiple valley degeneracy realize both high σ and high S, simultaneously. In addition, the bulks exhibited low κ_{lat} of 1.00 W m^{-1} K^{-1} for Ba_3SiO and 0.77 W m^{-1} K^{-1} for Ba_3GeO at RT, which is significantly lower than 8.2 W m^{-1} K^{-1} of normal perovskite $SrTiO_3$ bulk,[44] and even lower than 1.7–2.0 W m^{-1} K^{-1} of Bi_2Te_3 and PbTe bulks.[45–47] The low κ_{lat} of Ba_3BO originates from the low v_{ph} for phonons associated with Ba atomic vibration, and the phonons associated with Si and O atomic vibrations have a negligible contribution to κ_{lat} due to the very short τ_{ph}. The crystal structure of Ba_3BO is constructed from the highly distorted O–Ba_6 octahedra framework with weak O–Ba ionic bonds, which provides extremely low v_{ph} and strong phonon scattering. As a consequence of high PF and low κ_{lat}, the Ba_3SiO and Ba_3GeO exhibited rather high ZT of 0.16 and 0.35 at RT, respectively. The ZT value increased continuously up to 0.84 at T = 623 K for Ba_3SiO and 0.65 at T = 523 K for Ba_3GeO. In addition, based on first-principles carrier and phonon transport calculations, we predicted that a higher ZT could be obtained by optimizing hole concentration in Ba_3BO. Specifically, the maximum ZT potentially increases to 2.14 for Ba_3SiO and 1.21 for Ba_3GeO at T = 600 K. The present results indicate that inverse-perovskites would be a new platform of environmentally benign high ZT thermoelectric materials.

4. Experimental Section

Bulk Synthesis: The Ba_3SiO and Ba_3GeO bulk polycrystals were synthesized by solid-state reactions of a stoichiometric mixture of Ba, Si or Ge, and BaO via a reaction of 2Ba + Si(Ge) +BaO → $Ba_3SiO(Ba_3GeO)$. First, fresh Ba metal (purity 99.99%, Sigma–Aldrich) was finely cut into small pieces of grains.[137] The Ba grain, Si (purity 99.9%, Kojundo Chemical Lab.) or Ge powders (purity 99.9%, Kanto Chemical), and BaO powder (purity 99.9%, Kanto Chemical) were mixed and then pressed into 10-mmϕ pellet. The obtained pellet was wrapped in Ta foil and then sealed in an Ar-filled stainless tube. The sealed stainless tube was heated at an optimized temperature of 750 °C for 10 h for Ba_3SiO and 700 °C for 10 h for Ba_3GeO. The product was reground and densified to 10-mmϕ pellet again, and then it was wrapped in Ta foil and then sealed in an Ar-filled stainless tube. The sealed stainless tube was heated again at 900 °C for 10 h for Ba_3SiO and 700 °C for 10 h for Ba_3GeO. The bulk densities are 4.30 g cm^{-3} for Ba_3SiO and 4.35 g cm^{-3} for Ba_3GeO. The sintered densities are estimated to be 87.0% and 80.4%, respectively. The chemical compositions of the bulk samples measured with EDS are $Ba_{3.2}SiO_{1.6}$ and $Ba_{3.3}GeO_{1.5}$. The deviation from the stoichiometric composition would come from the coexistence of impurity phases, such as BaO, and the oxidation during sample transfer to measurement chamber. All the synthesis processes were performed in a glovebox with a dry inert Ar gas (the dew point < −100 °C, the oxygen concentration < 1 ppm).

Crystal Structure Analysis: Crystalline phases were determined by XRD with the Bragg–Brentano geometry with a Cu Kα radiation source at RT. The lattice parameters were determined by the Pawley method using the TOPAS ver. 4.2 program (Karlsruhe, Germany: Bruker AXS GmbH). Rietveld analysis, where the fundamental parameter (FP) method was employed, was performed for crystal structure refinement. The microstructure of the bulks was evaluated using a field-emission scanning electron microscopy (FE-SEM; JSM-7600F, JEOL) equipped with an energy-dispersive spectrometer (EDS). The electronic structures were characterized by X-ray photoemission spectroscopy (XPS) performed at the undulator beamline BL-2A of the Photon Factory, High Energy Accelerators Research Organization (KEK). The binding energy was calibrated with the Fermi level of an evaporated reference Au film. Diffuse reflectance (R) spectra were measured at RT with a spectrophotometer in the wavelength (λ) range of 200–2400 nm. The obtained R spectra were converted using the Kubelka–Munk function $(1-R)^2/(2R) = \alpha/S_f$, where α and S_f denote the optical absorption coefficient and the scattering factor, respectively, to obtain the quasi-optical absorption spectra.

Electronic and Thermal Properties: σ and S were simultaneously measured by the four-probe method (ZEM-3, ADVANCE RIKO, Inc.) under a He atmosphere. The κ was obtained from $\kappa = D{\cdot}C{\cdot}\rho$, where the thermal diffusivity (D) along the out-of-plane direction in the bulk was measured

in an Ar atmosphere by a laser flash diffusivity method (LFA 457, NETZSCH) and the heat capacity (C) was measured by differential scanning calorimetry (DSCvesta, Rigaku Corp.), and the sample density (ρ) was determined by the dimensions and mass of the samples. The sound velocity (ν_s) is obtained by $\nu_s = (\frac{1}{3}[\frac{2}{\nu_t^3} + \frac{1}{\nu_l^3}])^{-1/3}$, where ν_t and ν_l are the transverse and longitudinal sound velocities measured by ultrasonic pulse-echo method (1077DATA, KARL DEUTSCH) at RT. A detail of the phonon gas model analysis is described in the caption of Table S1 (Supporting Information).

Density Functional Theory Calculation: The electronic structure calculations were performed for Ba_3BO models by DFT conducted using the projector augmented wave (PAW) method as implemented in the VASP code.[34,35] Ba [5*d*6*s*6*p*], Si [3*s*3*p*], Ge [4*s*4*p*], and O [2*s*2*p*] orbitals were included as valence states. The variable-cell structure relaxations were performed by the generalized gradient approximation (GGA) Perdew–Burke–Ernzerhof (PBE) functional[138] with a plane wave cut-off energy of 550 eV, a Γ-centered k-mesh with the k-spacing of 0.2 $Å^{-1}$, as well as the convergence criteria of 10^{-6} eV for the energy and 0.01 eV $Å^{-1}$ for the force. The relaxed lattice parameters are a = 7.762 Å, b = 10.844 Å, c = 7.569 Å for Ba_3SiO and a = 7.761 Å, b = 10.888 Å, c = 7.608 Å for Ba_3GeO, in consistence with the experimentally obtained values within 3% differences. The electronic band structures and DOSs were obtained by the HSE hybrid functional.[36] The carrier effective masses were calculated by BoltzTraP2 code.[139] The carrier transport properties of Ba_3BO were calculated by using DFT and DFPT as implemented in the Quantum ESPRESSO package.[38,39] The GBRV ultrasoft pseudopotentials[140] were employed with the kinetic energy cutoff of 40 Ry (320 Ry) for wavefunctions (charge density). The k-mesh density of 6×4×6 was used for the DFT calculations, and the 2×2×2 q points were used for the phonon and electron-phonon calculations within DFPT. To compute the transport coefficients using dense k and q grids, the maximally localized Wannier functions (MLWFs) were constructed from the isolated 12 Kohn–Sham states below the VBM. The Wannierization was performed using the Wannier90 code,[141] where the Si (Ge) p orbitals were used as initial projections and the outer energy window of [−2.0, 0] eV relative to the VBM. The n, S, κ_{ele}, σ, and τ_e values at T = 300 K and 600 K were calculated using the PERTURBO code.[41] The electron–phonon coupling coefficients were interpolated to the dense 120×80×120 k and q points and then used to solve the Boltzmann transport equation within the relaxation time approximation (RTA). The carrier lifetimes were computed from the imaginary part of the Fan–Migdal self-energy, where the summation over the q points was performed by randomly sampling 10^6 q points from a uniform distribution. It was confirmed that the transport coefficients reached converged with the above parameters.

The phonon transport calculations for Ba_3BO were performed using the ALAMODE code.[51,52] A 2×2×2 supercell (160 atoms) was used for the calculation of harmonic interatomic force constants (IFCs) and the anharmonic IFCs. The harmonic IFCs were determined by the finite-displacement approach[142,143] and the anharmonic IFCs up to sixth-order were estimated by the compressive sensing lattice dynamics. The temperature-induced renormalized harmonic IFCs at T = 300 K were computed using the self-consistent phonon (SCPH) theory,[52] and were employed in the subsequent phonon transport calculations. All allowed interactions were included for the harmonic IFCs, the third-order IFCs inside the cutoff radii of 12 bohr, and fourth-, fifth-, and sixth-order IFCs inside the cutoff radii of 8 bohr. The DFT calculations to obtain the force were performed using the GGA-PBE functional with a plane-wave energy cutoff of 400 eV, a Γ-centered 2×2×1 k-mesh and an energy convergence criterion of 10^{-8} eV. κ_{lat} was calculated by solving the Peierls–Boltzmann transport equation under the RTA with a 7×7×5 q point mesh, which provides sufficient accuracy confirmed by the convergence tests (Figure S6, Supporting Information). The non-analytic correction was included to the dynamical matrix by the mixed-space approach,[144] in which the Born effective charges of constituent elements and the dielectric constants were obtained by DFPT.[37]

CCDC 2291770 and 2291771 contain the supplementary crystallographic data for this paper. These data can be obtained free of charge from The Cambridge Crystallographic Data Centre via www.ccdc.cam.ac.uk/data_request/cif.

Supporting Information

Supporting Information is available from the Wiley Online Library or from the author.

Acknowledgements

The authors thank Mr. Tatsuya Cho (Tokyo Institute of Technology, Japan) for supporting initial experiment and valuable discussion. This work was supported by MEXT Program: Data Creation and Utilization Type Material Research and Development Project Grant Number JPMXP1122683430. Ta.K. was supported by Japan Society for the Promotion of Science (JSPS) through Grants-in-Aid for Scientific Research (B) (Grant No. JP22H01766), Scientific Research (S) (Grant No. JP22H04964), and Challenging Research (Exploratory) (Grant No. JP22K18881). T.T. was supported by JSPS through Grant-in-Aid for Scientific Research (C) (Grant No. JP21K03424). H.Hi. was supported by JSPS through Grants-in-Aid for Scientific Research (A) (Grant Nos. JP20H00302 and JP21H04612). The numerical calculations were carried out on the TSUBAME3.0 supercomputer at Tokyo Institute of Technology supported by the MEXT Project of the Tokyo Tech Academy for Convergence of Materials and Informatics (TAC-MI). The crystal structures in Figures 1 and 2a were drawn using the VESTA code.[145]

Conflict of Interest

The authors declare no conflict of interest.

Data Availability Statement

The data that support the findings of this study are available from the corresponding author upon reasonable request.

Keywords

electronic transport, material design, phonon scattering, semiconductor, thermoelectric material

Received: September 25, 2023
Revised: November 19, 2023
Published online: December 25, 2023

[1] F. J. Disalvo, *Science* **1999**, *285*, 703.
[2] L. E. Bell, *Science* **2008**, *321*, 1457.
[3] Q. H. Zhang, X. Y. Huang, S. Q. Bai, X. Shi, C. Uher, L. D. Chen, *Adv. Eng. Mater.* **2016**, *18*, 194.
[4] G. J. Snyder, E. S. Toberer, *Nat. Mater.* **2008**, *7*, 105.
[5] J. He, T. M. Tritt, *Science* **2017**, *357*, eaak9997.
[6] T. Zhu, Y. Liu, C. Fu, J. P. Heremans, J. G. Snyder, X. Zhao, *Adv. Mater.* **2017**, *29*, 1605884.
[7] J. Li, X. Zhang, Z. Chen, S. Lin, W. Li, J. Shen, I. T. Witting, A. Faghaninia, Y. Chen, A. Jain, L. Chen, G. J. Snyder, Y. Pei, *Joule* **2018**, *2*, 976.
[8] Y. Xiao, L.-D. Zhao, *npj Quantum Mater.* **2018**, *3*, 55.
[9] I. T. Witting, T. C. Chasapis, F. Ricci, M. Peters, N. A. Heinz, G. Hautier, G. J. Snyder, *Adv. Electron. Mater.* **2019**, *5*, 1800904.

[10] I. Terasaki, *APL Mater.* **2016**, *4*, 104501.
[11] W.-D. Liu, L. Yang, Z.-G. Chen, J. Zou, *Adv. Mater.* **2020**, *32*, 1905703.
[12] K. Xia, C. Hu, C. Fu, X. Zhao, T. Zhu, *Appl. Phys. Lett.* **2021**,*118*, 140503.
[13] A. Nozariasbmarz, A. Agarwal, Z. A. Coutant, M. J. Hall, J. Liu, R. Liu, A. Malhotra, P. Norouzzadeh, M. C. Öztürk, V. P. Ramesh, Y. Sargolzaeiaval, F. Suarez, D. Vashaee, *Jpn. J. Appl. Phys.* **2017**, *56*, 05DA04.
[14] O. Caballero-Calero, J. R. Ares, M. Martín-González, *Adv. Sustainable Syst.* **2021**, *5*, 2100095.
[15] A. Widera, H. Schäfer, *Mater. Res. Bull.* **1980**, *15*, 1805.
[16] A. Widera, H. Schäfer, *J. Less-Common Met.* **1981**, *77*, 29.
[17] C. Röhr, *Z. Kristallogr.* **1995**, *210*, 781.
[18] B. Huang, J. D. Corbett, *Z. Anorg. Allg. Chem.* **1998**, *624*, 1787.
[19] A. Velden, M. Jansen, *Z. Anorg. Allg. Chem.* **2004**, *630*, 234.
[20] M. Kirchner, W. Schnelle, R. Niewa, *Z. Anorg. Allg. Chem.* **2006**, *632*, 559.
[21] Y. Suemune, *J Phys. Soc. Jpn.* **1965**, *20*, 174.
[22] T. Kariyado, M. Ogata, *J. Phys. Soc. Jpn.* **2011**, *80*, 083704.
[23] T. Kariyado, M. Ogata, *J. Phys. Soc. Jpn.* **2012**, *81*, 064701.
[24] T. H. Hsieh, J. Liu, L. Fu, *Phys. Rev. B* **2014**, *90*, 081112.
[25] M. Oudah, J. N. Hausmann, S. Kitao, A. Ikeda, S. Yonezawa, M. Seto, Y. Maeno, *Sci. Rep.* **2019**, *9*, 1831.
[26] Y. Obata, R. Yukawa, K. Horiba, H. Kumigashira, Y. Toda, S. Matsuishi, H. Hosono, *Phys. Rev. B* **2017**, *96*, 155109.
[27] Y. Okamoto, A. Sakamaki, K. Takenaka, *J. Appl. Phys.* **2016**, *119*, 205106.
[28] Q. Mahmood, A. Ashraf, M. Hassan, *Indian J. Phys.* **2018**, *92*, 865.
[29] M. Ochi, K. Kuroki, *Phys. Rev. Appl.* **2019**, *12*, 034009.
[30] A. C. Garcia-Castro, R. Ospina, J. H. Quintero, *J. Phys. Chem. Solids* **2020**, *136*, 109126.
[31] J. Nuss, C. Mühle, K. Hayama, V. Abdolazimi, H. Takagi, *Acta Cryst* **2015**, *B71*, 300.
[32] N. Ohashi, D. Mora-Fonz, S. Otani, T. Ohgaki, M. Miyakawa, A. Shluger, *Inorg. Chem.* **2020**, *59*, 18305.
[33] J.-H. Pöhls, A. Mar, *J. Appl. Phys.* **2019**, *126*, 025110.
[34] G. Kresse, D. Joubert, *Phys. Rev. B* **1999**, *59*, 1758.
[35] G. Kresse, J. Furthmüller, *Phys. Rev. B* **1996**, *54*, 11169.
[36] J. Heyd, G. E. Scuseria, M. Ernzerhof, *J. Chem. Phys.* **2003**, *118*, 8207.
[37] S. Baroni, S. De Gironcoli, A. Dal Corso, P. Giannozzi, *Rev. Mod. Phys.* **2001**, *73*, 515.
[38] P. Giannozzi, S. Baroni, N. Bonini, M. Calandra, R. Car, C. Cavazzoni, D. Ceresoli, G. L. Chiarotti, M. Cococcioni, I. Dabo, A. Dal Corso, S. De Gironcoli, S. Fabris, G. Fratesi, R. Gebauer, U. Gerstmann, C. Gougoussis, A. Kokalj, M. Lazzeri, L. Martin-Samos, N. Marzari, F. Mauri, R. Mazzarello, S. Paolini, A. Pasquarello, L. Paulatto, C. Sbraccia, S. Scandolo, G. Sclauzero, A. P. Seitsonen, et al., *J Phys Condens Matter* **2009**, *21*, 395502.
[39] P. Giannozzi, O. Andreussi, T. Brumme, O. Bunau, M. Buongiorno Nardelli, M. Calandra, R. Car, C. Cavazzoni, D. Ceresoli, M. Cococcioni, N. Colonna, I. Carnimeo, A. Dal Corso, S. De Gironcoli, P. Delugas, R. A. Distasio, A. Ferretti, A. Floris, G. Fratesi, G. Fugallo, R. Gebauer, U. Gerstmann, F. Giustino, T. Gorni, J. Jia, M. Kawamura, H.-Y. Ko, A. Kokalj, et al., *J Phys Condens Matter* **2017**, *29*, 465901.
[40] J.-J. Zhou, J. Park, I.-T. Lu, I. Maliyov, X. Tong, M. Bernardi, *Comput. Phys. Commun.* **2021**, *264*, 107970.
[41] G. J. Snyder, A. H. Snyder, M. Wood, R. Gurunathan, B. H. Snyder, C. Niu, *Adv. Mater.* **2020**, *32*, 2001537.
[42] J. Y. W. Seto, *J. Appl. Phys.* **1975**, *46*, 5247.
[43] J. Ravichandran, W. Siemons, M. L. Scullin, S. Mukerjee, M. Huijben, J. E. Moore, A. Majumdar, R. Ramesh, *Phys. Rev. B* **2011**, *83*, 035101.
[44] X. He, S. Nomoto, T. Komatsu, T. Katase, T. Tadano, S. Kitani, H. Yoshida, T. Yamamoto, H. Mizoguchi, K. Ide, H. Hiramatsu, H. Kawaji, H. Hosono, T. Kamiya, *Adv. Funct. Mater.* **2023**, 2213144.
[45] C. B. Satterthwaite, R. W. Ure Jr., *Phys. Rev.* **1957**, *108*, 1164.
[46] H. J. Goldsmid, *J. Appl. Phys.* **1961**, *32*, 2198.
[47] A. A. El-Sharkawy, A. M. Abou El-Azm, M. I. Kenawy, A. S. Hillal, H. M. Abu-Basha, *Int. J. Thermophys.* **1983**, *4*, 261.
[48] C. Zhou, Y. K. Lee, Y. Yu, S. Byun, Z.-Z. Luo, H. Lee, B. Ge, Y.-L. Lee, X. Chen, J. Y. Lee, O. Cojocaru-Mirédin, H. Chang, J. Im, S.-P. Cho, M. Wuttig, V. P. Dravid, M. G. Kanatzidis, *Nat. Mater.* **2021**, *20*, 1378.
[49] A. A. Olvera, N. A. Moroz, P. Sahoo, P. Ren, T. P. Bailey, A. A. Page, C. Uher, P. F. P. Poudeu, *Energy Environ. Sci.* **2017**, *10*, 1668.
[50] E. S. Toberer, A. Zevalkink, G. J. Snyder, *J. Mater. Chem.* **2011**, *21*, 15843.
[51] T. Tadano, S. Tsuneyuki, *Phys. Rev. B* **2015**, *92*, 054301.
[52] T. Tadano, Y. Gohda, S. Tsuneyuki, *J. Phys.: Condens. Matter* **2014**, *26*, 225402.
[53] R. Dronskowski, P. E. Bloechl, *J. Phys. Chem.* **1993**, *97*, 8617.
[54] S. Maintz, V. L. Deringer, A. L. Tchougréeff, R. Dronskowski, *J. Comput. Chem.* **2016**, *37*, 1030.
[55] S. Zheng, S. Xiao, K. Peng, Y. Pan, X. Yang, X. Lu, G. Han, B. Zhang, Z. Zhou, G. Wang, X. Zhou, *Adv. Mater.* **2023**, *35*, 2210380.
[56] Y. He, T. Day, T. Zhang, H. Liu, X. Shi, L. Chen, G. J. Snyder, *Adv. Mater.* **2014**, *26*, 3974.
[57] Q.-L. Meng, S. Kong, Z. Huang, Y. Zhu, H.-C. Liu, X. Lu, P. Jiang, X. Bao, *J. Mater. Chem. A* **2016**, *4*, 12624.
[58] H. Tang, F.-H. Sun, J.-F. Dong, Asfandiyar, H.-L. Zhuang, Y. Pan, J.-F. Li, *Nano Energy* **2018**, *49*, 267.
[59] Z.-H. Ge, Y.-X. Zhang, D. Song, X. Chong, P. Qin, F. Zheng, J. Feng, L.-D. Zhao, *J. Mater. Chem. A* **2018**, *6*, 14440.
[60] H. Q. Yang, X. Y. Wang, H. Wu, B. Zhang, D. D. Xie, Y. J. Chen, X. Lu, X. D. Han, L. Miao, X. Y. Zhou, *J. Mater. Chem. C* **2019**, *7*, 3351.
[61] E. Guilmeau, Y. Bréard, A. Maignan, *Appl. Phys. Lett.* **2011**, *99*, 052107.
[62] Y. Li, T. Zhang, Y. Qin, T. Day, G. Jeffrey Snyder, X. Shi, L. Chen, *J. Appl. Phys.* **2014**, *116*, 203705.
[63] T. Deng, P. Qiu, T. Xing, Z. Zhou, T.-R. Wei, D. Ren, J. Xiao, X. Shi, L. Chen, *J. Mater. Chem. A* **2021**, *9*, 7946.
[64] G. Guélou, A. V. Powell, P. Vaqueiro, *J. Mater. Chem. C* **2015**, *3*, 10624.
[65] Y. Kikuchi, Y. Bouyrie, M. Ohta, K. Suekuni, M. Aihara, T. Takabatake, *J. Mater. Chem. A* **2016**, *4*, 15207.
[66] A. Nagaoka, K. Yoshino, T. Masuda, T. D. Sparks, M. A. Scarpulla, K. Nishioka, *J. Mater. Chem. A* **2021**, *9*, 15595.
[67] X. W. Wang, H. Lee, Y. C. Lan, G. H. Zhu, G. Joshi, D. Z. Wang, J. Yang, A. J. Muto, M. Y. Tang, J. Klatsky, S. Song, M. S. Dresselhaus, G. Chen, Z. F. Ren, *Appl. Phys. Lett.* **2008**, *93*, 193121.
[68] X. Chen, J. Zhou, J. B. Goodenough, L. Shi, *J. Mater. Chem. C* **2015**, *3*, 10500.
[69] S. Muthiah, R. C. Singh, B. D. Pathak, P. K. Avasthi, R. Kumar, A. Kumar, A. K. Srivastava, A. Dhar, *Nanoscale* **2018**, *10*, 1970.
[70] Z. Gao, Z. Xiong, J. Li, C. Lu, G. Zhang, T. Zeng, Y. Ma, G. Ma, R. Zhang, K. Chen, T. Zhang, Y. Liu, J. Yang, L. Cao, K. Jin, *J. Mater. Chem. A* **2019**, *7*, 3384.
[71] W. Liu, X. Tan, K. Yin, H. Liu, X. Tang, J. Shi, Q. Zhang, C. Uher, *Phys. Rev. Lett.* **2012**, *108*, 166601.
[72] Z. Zamanipour, X. Shi, M. Mozafari, J. S. Krasinski, L. Tayebi, D. Vashaee, *Ceram. Int.* **2013**, *39*, 2353.
[73] H. Nakasawa, T. Takamatsu, Y. Iijima, K. Hayashi, Y. Miyazaki, *Trans. Mater. Res. Soc. Jpn.* **2018**, 43.
[74] M. Mohebali, Y. Liu, L. Tayebi, J. S. Krasinski, D. Vashaee, *Renewable Energy* **2015**, *74*, 940.
[75] Y.-K. Kuo, B. Ramachandran, C.-S. Lue, *Front Chem* **2014**, *2*, 106.

[76] J. Wang, B.-Y. Zhang, H.-J. Kang, Y. Li, X. Uaer, J.-F. Li, Q. Tan, S. Zhang, G.-H. Fan, C.-Y. Liu, L. Miao, D. Nan, T.-M. Wang, L.-D. Zhao, *Nano Energy* **2017**, *35*, 387.
[77] J.-B. Li, J. Wang, J.-F. Li, Y. Li, H. Yang, H.-Y. Yu, X.-B. Ma, X. Yaer, L. Liu, L. Miao, *J. Mater. Chem. C* **2018**, *6*, 7594.
[78] Z. Lu, H. Zhang, W. Lei, D. C. Sinclair, I. M. Reaney, *Chem. Mater.* **2016**, *28*, 925.
[79] M. Ohtaki, K. Araki, K. Yamamoto, *J. Electron. Mater.* **2009**, *38*, 1234.
[80] M. Ito, *Scripta Mater* **2003**, *48*, 403.
[81] N. Van Nong, N. Pryds, S. Linderoth, M. Ohtaki, *Adv. Mater.* **2011**, *23*, 2484.
[82] C.-O. Romo-De-La-Cruz, Y. Chen, L. Liang, M. Williams, X. Song, *Chem. Mater.* **2020**, *32*, 9730.
[83] R. J. Mehta, Y. Zhang, C. Karthik, B. Singh, R. W. Siegel, T. Borca-Tasciuc, G. Ramanath, *Nat. Mater.* **2012**, *11*, 233.
[84] T. Zhu, Z. Xu, J. He, J. Shen, S. Zhu, L. Hu, T. M. Tritt, X. Zhao, *J. Mater. Chem. A* **2013**, *1*, 11589.
[85] L. Hu, T. Zhu, X. Liu, X. Zhao, *Adv. Funct. Mater.* **2014**, *24*, 5211.
[86] S. I. Kim, K. H. Lee, H. A. Mun, H. S. Kim, S. W. Hwang, J. W. Roh, D. J. Yang, W. H. Shin, X. S. Li, Y. H. Lee, G. J. Snyder, S. W. Kim, *Science* **2015**, *348*, 109.
[87] B. Du, H. Li, J. Xu, X. Tang, C. Uher, *Chem. Mater.* **2010**, *22*, 5521.
[88] M. Hong, Z.-G. Chen, L. Yang, Z.-M. Liao, Y.-C. Zou, Y.-H. Chen, S. Matsumura, J. Zou, *Adv. Energy Mater.* **2018**, *8*, 1702333.
[89] S. Perumal, S. Roychowdhury, K. Biswas, *Inorg. Chem. Front.* **2016**, *3*, 125.
[90] M. Hong, Z.-G. Chen, L. Yang, Y.-C. Zou, M. S. Dargusch, H. Wang, J. Zou, *Adv. Mater.* **2018**, *30*, 1705942.
[91] J. Li, X. Zhang, X. Wang, Z. Bu, L. Zheng, B. Zhou, F. Xiong, Y. Chen, Y. Pei, *J. Am. Chem. Soc.* **2018**, *140*, 16190.
[92] Z. Liu, J. Sun, J. Mao, H. Zhu, W. Ren, J. Zhou, Z. Wang, D. J. Singh, J. Sui, C.-W. Chu, Z. Ren, *Proc. Natl. Acad. Sci. USA* **2018**, *115*, 5332.
[93] X. Zhang, J. Li, X. Wang, Z. Chen, J. Mao, Y. Chen, Y. Pei, *J. Am. Chem. Soc.* **2018**, *140*, 15883.
[94] Z. Zheng, X. Su, R. Deng, C. Stoumpos, H. Xie, W. Liu, Y. Yan, S. Hao, C. Uher, C. Wolverton, M. G. Kanatzidis, X. Tang, *J. Am. Chem. Soc.* **2018**, *140*, 2673.
[95] B. Srinivasan, A. Gellé, F. Gucci, C. Boussard-Pledel, B. Fontaine, R. Gautier, J.-F. Halet, M. J. Reece, B. Bureau, *Inorg. Chem. Front.* **2019**, *6*, 63.
[96] M. Hong, Y. Wang, T. Feng, Q. Sun, S. Xu, S. Matsumura, S. T. Pantelides, J. Zou, Z.-G. Chen, *J. Am. Chem. Soc.* **2019**, *141*, 1742.
[97] L.-D. Zhao, S.-H. Lo, Y. Zhang, H. Sun, G. Tan, C. Uher, C. Wolverton, V. P. Dravid, M. G. Kanatzidis, *Nature* **2014**, *508*, 373.
[98] L.-D. Zhao, G. Tan, S. Hao, J. He, Y. Pei, H. Chi, H. Wang, S. Gong, H. Xu, V. P. Dravid, C. Uher, G. J. Snyder, C. Wolverton, M. G. Kanatzidis, *Science* **2016**, *351*, 141.
[99] K. Peng, X. Lu, H. Zhan, S. Hui, X. Tang, G. Wang, J. Dai, C. Uher, G. Wang, X. Zhou, *Energy Environ. Sci.* **2016**, *9*, 454.
[100] S. Liang, J. Xu, J. G. Noudem, H. Wang, X. Tan, G.-Q. Liu, H. Shao, B. Yu, S. Yue, J. Jiang, *J. Mater. Chem. A* **2018**, *6*, 23730.
[101] J. Liu, P. Wang, M. Wang, R. Xu, J. Zhang, J. Liu, D. Li, N. Liang, Y. Du, G. Chen, G. Tang, *Nano Energy* **2018**, *53*, 683.
[102] X. Shi, K. Zheng, M. Hong, W. Liu, R. Moshwan, Y. Wang, X. Qu, Z.-G. Chen, J. Zou, *Chem. Sci.* **2018**, *9*, 7376.
[103] X. Shi, A. Wu, T. Feng, K. Zheng, W. Liu, Q. Sun, M. Hong, S. T. Pantelides, Z.-G. Chen, J. Zou, *Adv. Energy Mater.* **2019**, *9*, 1803242.
[104] Y. Luo, S. Cai, X. Hua, H. Chen, Q. Liang, C. Du, Y. Zheng, J. Shen, J. Xu, C. Wolverton, V. P. Dravid, Q. Yan, M. G. Kanatzidis, *Adv. Energy Mater.* **2019**, *9*, 1803072.
[105] Q. Zhang, B. Liao, Y. Lan, K. Lukas, W. Liu, K. Esfarjani, C. Opeil, D. Broido, G. Chen, Z. Ren, *Proc. Natl. Acad. Sci. USA* **2013**, *110*, 13261.
[106] G. Tan, F. Shi, S. Hao, H. Chi, T. P. Bailey, L.-D. Zhao, C. Uher, C. Wolverton, V. P. Dravid, M. G. Kanatzidis, *J. Am. Chem. Soc.* **2015**, *137*, 11507.
[107] L.-D. Zhao, X. Zhang, H. Wu, G. Tan, Y. Pei, Y. Xiao, C. Chang, D. Wu, H. Chi, L. Zheng, S. Gong, C. Uher, J. He, M. G. Kanatzidis, *J. Am. Chem. Soc.* **2016**, *138*, 2366.
[108] R. Al Rahal Al Orabi, N. A. Mecholsky, J. Hwang, W. Kim, J.-S. Rhyee, D. Wee, M. Fornari, *Chem. Mater.* **2016**, *28*, 376.
[109] W. Li, L. Zheng, B. Ge, S. Lin, X. Zhang, Z. Chen, Y. Chang, Y. Pei, *Adv. Mater.* **2017**, *29*, 1605887.
[110] L. Hu, Y. Zhang, H. Wu, J. Li, Y. Li, M. Mckenna, J. He, F. Liu, S. J. Pennycook, X. Zeng, *Adv. Energy Mater.* **2018**, *8*, 1802116.
[111] Z. Zhou, J. Yang, Q. Jiang, X. Lin, J. Xin, A. Basit, J. Hou, B. Sun, *Nano Energy* **2018**, *47*, 81.
[112] A. Banik, T. Ghosh, R. Arora, M. Dutta, J. Pandey, S. Acharya, A. Soni, U. V. Waghmare, K. Biswas, *Energy Environ. Sci.* **2019**, *12*, 589.
[113] L.-D. Zhao, J. He, C.-I. Wu, T. P. Hogan, X. Zhou, C. Uher, V. P. Dravid, M. G. Kanatzidis, *J. Am. Chem. Soc.* **2012**, *134*, 7902.
[114] L.-D. Zhao, J. He, S. Hao, C.-I. Wu, T. P. Hogan, C. Wolverton, V. P. Dravid, M. G. Kanatzidis, *J. Am. Chem. Soc.* **2012**, *134*, 16327.
[115] Q. Zhang, F. Cao, W. Liu, K. Lukas, B. Yu, S. Chen, C. Opeil, D. Broido, G. Chen, Z. Ren, *J. Am. Chem. Soc.* **2012**, *134*, 10031.
[116] L.-D. Zhao, S. Hao, S.-H. Lo, C.-I. Wu, X. Zhou, Y. Lee, H. Li, K. Biswas, T. P. Hogan, C. Uher, C. Wolverton, V. P. Dravid, M. G. Kanatzidis, *J. Am. Chem. Soc.* **2013**, *135*, 7364.
[117] L. D. Zhao, H. J. Wu, S. Q. Hao, C. I. Wu, X. Y. Zhou, K. Biswas, J. Q. He, T. P. Hogan, C. Uher, C. Wolverton, V. P. Dravid, M. G. Kanatzidis, *Energy Environ. Sci.* **2013**, *6*, 3346.
[118] H. J. Wu, L.-D. Zhao, F. S. Zheng, D. Wu, Y. L. Pei, X. Tong, M. G. Kanatzidis, J. Q. He, *Nat. Commun.* **2014**, *5*, 4515.
[119] R. J. Korkosz, T. C. Chasapis, S.-H. Lo, J. W. Doak, Y. J. Kim, C.-I. Wu, E. Hatzikraniotis, T. P. Hogan, D. N. Seidman, C. Wolverton, V. P. Dravid, M. G. Kanatzidis, *J. Am. Chem. Soc.* **2014**, *136*, 3225.
[120] G. Tan, F. Shi, S. Hao, L.-D. Zhao, H. Chi, X. Zhang, C. Uher, C. Wolverton, V. P. Dravid, M. G. Kanatzidis, *Nat. Commun.* **2016**, *7*, 12167.
[121] J. M. Hodges, S. Hao, J. A. Grovogui, X. Zhang, T. P. Bailey, X. Li, Z. Gan, Y.-Y. Hu, C. Uher, V. P. Dravid, C. Wolverton, M. G. Kanatzidis, *J. Am. Chem. Soc.* **2018**, *140*, 18115.
[122] H. Liu, X. Shi, F. Xu, L. Zhang, W. Zhang, L. Chen, Q. Li, C. Uher, T. Day, G. J. Snyder, *Nat. Mater.* **2012**, *11*, 422.
[123] L. Yang, Z.-G. Chen, G. Han, M. Hong, Y. Zou, J. Zou, *Nano Energy* **2015**, *16*, 367.
[124] Y. He, P. Lu, X. Shi, F. Xu, T. Zhang, G. J. Snyder, C. Uher, L. Chen, *Adv. Mater.* **2015**, *27*, 3639.
[125] K. Zhao, H. Duan, N. Raghavendra, P. Qiu, Y. Zeng, W. Zhang, J. Yang, X. Shi, L. Chen, *Adv. Mater.* **2017**, *29*, 1701148.
[126] R. Nunna, P. Qiu, M. Yin, H. Chen, R. Hanus, Q. Song, T. Zhang, M.-Y. Chou, M. T. Agne, J. He, G. J. Snyder, X. Shi, L. Chen, *Energy Environ. Sci.* **2017**, *10*, 1928.
[127] K. Zhao, C. Zhu, P. Qiu, A. B. Blichfeld, E. Eikeland, D. Ren, B. B. Iversen, F. Xu, X. Shi, L. Chen, *Nano Energy* **2017**, *42*, 43.
[128] L. Zhao, S. M. K. N. Islam, J. Wang, D. L. Cortie, X. Wang, Z. Cheng, J. Wang, N. Ye, S. Dou, X. Shi, L. Chen, G. J. Snyder, X. Wang, *Nano Energy* **2017**, *41*, 164.
[129] M. Li, D. L. Cortie, J. Liu, D. Yu, S. M. d. K. N. Islam, L. Zhao, D. R. G. Mitchell, R. A. Mole, M. B. Cortie, S. Dou, X. Wang, *Nano Energy* **2018**, *53*, 993.
[130] C. Fu, S. Bai, Y. Liu, Y. Tang, L. Chen, X. Zhao, T. Zhu, *Nat. Commun.* **2015**, *6*, 8144.
[131] C. Fu, T. Zhu, Y. Liu, H. Xie, X. Zhao, *Energy Environ. Sci.* **2015**, *8*, 216.
[132] J. Yu, C. Fu, Y. Liu, K. Xia, U. Aydemir, T. C. Chasapis, G. J. Snyder, X. Zhao, T. Zhu, *Adv. Energy Mater.* **2018**, *8*, 1701313.

[133] L. D. Zhao, D. Berardan, Y. L. Pei, C. Byl, L. Pinsard-Gaudart, N. Dragoe, *Appl. Phys. Lett.* **2010**, *97*, 092118.
[134] J. Li, J. Sui, Y. Pei, C. Barreteau, D. Berardan, N. Dragoe, W. Cai, J. He, L.-D. Zhao, *Energy Environ. Sci.* **2012**, *5*, 8543.
[135] J. Heo, G. Laurita, S. Muir, M. A. Subramanian, D. A. Keszler, *Chem. Mater.* **2014**, *26*, 2047.
[136] T. Barbier, P. Lemoine, S. Gascoin, O. I. Lebedev, A. Kaltzoglou, P. Vaqueiro, A. V. Powell, R. I. Smith, E. Guilmeau, *J. Alloys Compd.* **2015**, *634*, 253.
[137] T. Katase, H. Hiramatsu, T. Kamiya, H. Hosono, *Appl. Phys. Express* **2010**, *3*, 063101.
[138] J. P. Perdew, K. Burke, M. Ernzerhof, *Phys. Rev. Lett.* **1996**, *77*, 3865.
[139] G. K. H. Madsen, J. Carrete, M. J. Verstraete, *Comput. Phys. Commun.* **2018**, *231*, 140.
[140] K. F. Garrity, J. W. Bennett, K. M. Rabe, D. Vanderbilt, *Comput. Mater. Sci.* **2014**, *81*, 446.
[141] G. Pizzi, V. Vitale, R. Arita, S. Blügel, F. Freimuth, G. Géranton, M. Gibertini, D. Gresch, C. Johnson, T. Koretsune, J. Ibañez-Azpiroz, H. Lee, J.-M. Lihm, D. Marchand, A. Marrazzo, Y. Mokrousov, J. I. Mustafa, Y. Nohara, Y. Nomura, L. Paulatto, S. Poncé, T. Ponweiser, J. Qiao, F. Thöle, S. S. Tsirkin, M. Wierzbowska, N. Marzari, D. Vanderbilt, I. Souza, A. A. Mostofi, *et al. J Phys Condens Matter* **2019**, *32*, 165902.
[142] G. Kresse, J. Furthmüller, J. Hafner, *Europhys. Lett.* **1995**, *32*, 729.
[143] K. Parlinski, Z. Q. Li, Y. Kawazoe, *Phys. Rev. Lett.* **1997**, *78*, 4063.
[144] Y. Wang, J. J. Wang, W. Y. Wang, Z. G. Mei, S. L. Shang, L. Q. Chen, Z. K. Liu, *J Phys Condens Matter* **2010**, *22*, 202201.
[145] K. Momma, F. Izumi, *J. Appl. Crystallogr.* **2011**, *44*, 1272.

